A robust method for selecting a high-quality interferogram subset in InSAR surface deformation analysis

Molly S Zebker[1] and Jingyi Chen[2]

[1]The University of Texas at Austin
[2]University of Texas at Austin

April 16, 2024

Abstract

The accuracy of surface deformation derived from Interferometric Synthetic Aperture Radar (InSAR) observations depends on the quality of the chosen interferogram subset. We present a method to select interferogram subsets based on unwrapping errors rather than temporal baseline thresholds. Using Sentinel-1 interferograms over the Tulare Basin (CA), we show that tropospheric noise dominates short temporal baseline subset solutions (with up to 2.9 cm/yr residuals at co-located GPS sites), while decorrelation leads to a systematic underestimation of true deformation rate in long temporal baseline subset solutions (with up to 5.5 cm/yr residuals). Our new workflow better mitigates these two noise sources at the same time. In the Eagle Ford (TX) region, our strategy revealed up to ~11 cm of cumulative line-of-sight (LOS) deformation over a ~900 km2 region. This deformation feature is associated with ongoing oil and gas activities and is reported for the first time here.

A robust method for selecting a high-quality interferogram subset in InSAR surface deformation analysis

M. S. Zebker [1*], J. Chen[1,2]

[1]Jackson School of Geosciences, Department of Earth and Planetary Science, The University of Texas at Austin, Austin, TX
[2]Department of Aerospace Engineering and Engineering Mechanics, The University of Texas at Austin, Austin, TX

Key Points:

- InSAR phase coherence does not always decrease with temporal baselines.
- Choosing interferograms based on phase quality rather than temporal baselines better mitigates decorrelation and tropospheric noise.
- The improved InSAR analysis strategy reveals up to 11 cm of deformation signals associated with oil and gas operations over the Eagle Ford.

*Austin, TX

Corresponding author: Molly S. Zebker, mzebker@utexas.edu

Abstract

The accuracy of surface deformation derived from Interferometric Synthetic Aperture Radar (InSAR) observations depends on the quality of the chosen interferogram subset. We present a method to select interferogram subsets based on unwrapping errors rather than temporal baseline thresholds. Using Sentinel-1 interferograms over the Tulare Basin (CA), we show that tropospheric noise dominates short temporal baseline subset solutions (with up to 2.9 cm/yr residuals at co-located GPS sites), while decorrelation leads to a systematic underestimation of true deformation rate in long temporal baseline subset solutions (with up to 5.5 cm/yr residuals). Our new workflow better mitigates these two noise sources at the same time. In the Eagle Ford (TX) region, our strategy revealed up to ∼11 cm of cumulative line-of-sight (LOS) deformation over a ∼900 km^2 region. This deformation feature is associated with ongoing oil and gas activities and is reported for the first time here.

Plain Language Summary

Deformation estimates are often impacted by noise related to weather conditions and surface vegetation changes. It is common to select an interferogram subset based on a temporal baseline threshold. However, InSAR phase quality may be influenced by other factors such as the weather conditions and surface vegetation rather than temporal baselines. We designed an InSAR processing strategy and applied it to two vegetated regions that experience land subsidence due to agriculture groundwater pumping or oil and gas production. In the Tulare Basin, we showed that deformation estimates are impacted by weather and vegetation related noise and can vary substantially depending on which interferograms are chosen. With our strategy, we better mitigate both noise sources at the same time. In the Eagle Ford region, our workflow revealed up to ∼11 cm of surface deformation over a ∼900 km^2 area for the first time. This is an oil and gas producing region where production activities have led to an increase in seismicity. Based on these findings, accurate surface deformation derived from InSAR data is now achievable in densely vegetated regions and can play an important role in future induced seismicity studies.

1 Introduction

Interferometric Synthetic Aperture Radar (InSAR) is an imaging radar technique for measuring surface deformation associated with geophysical processes including, but not limited to, tectonics (e.g., Fialko et al., 2002; Wright et al., 2004; Shirzaei & Bürgmann, 2013; Fielding et al., 2017; Xu et al., 2021), volcanism (e.g., Jónsson et al., 2000; Pritchard & Simons, 2002; Hooper et al., 2004; Lundgren et al., 2013), and groundwater hydrology (e.g., Amelung et al., 1999; Hoffmann et al., 2001; Schmidt & Burgmann, 2003; Bell et al., 2008; Chaussard et al., 2014). Achieving millimeter-to-centimeter level accuracy required by many of these studies, however, is challenging due to effects such as decorrelation and atmospheric artifacts. Physical changes in the surface properties between two radar image acquisitions (e.g., vegetation growth and surface disturbance) lead to phase decorrelation (H. A. Zebker & Villasenor, 1992). Phase measurements at completely decorrelated radar pixels do not contain spatially coherent phase information. Conversely, changes in temperature, pressure, and humidity (Bevis et al., 1992) often appear as spatially coherent tropospheric noise, similar to surface deformation signals. While weather models and topography data can be used to estimate and remove the stratified tropospheric noise component (e.g., Doin et al., 2009; Wadge et al., 2002; Jolivet et al., 2011; Li et al., 2009; Bekaert et al., 2015a, 2015b), these approaches often fail to capture the turbulent noise component that is approximately random at time scales greater than a day (Emardson et al., 2003). In many InSAR studies, decorrelation and tropospheric turbulence noise are the two major factors that limit InSAR measurement accuracy.

To mitigate tropospheric and decorrelation noise, Berardino et al. (2002) developed the Small BAseline Subset (SBAS) method to derive surface deformation solutions from a stack of interferograms. The algorithm assumes that interferograms with large temporal baselines (the time between two radar acquisitions used to form the interferogram) often suffer from more severe decorrelation artifacts. Therefore, the use of a temporal baseline threshold in the subset selection can reduce the number of decorrelated phase measurements used in surface deformation analysis. A problem arises in areas with dense vegetation where phase decorrelation occurs even in short baseline interferograms (e.g., 48 or 60 days), which limits the interferogram subset size and ability to reduce other noise terms. To better mitigate decorrelation noise, Persistent Scatterer (PS) algorithms were developed to select pixels that suffer from minimal decorrelation artifacts (e.g., roads, buildings, or bare rock) (e.g., Ferretti et al., 2000; Hooper et al., 2004; Agram, 2010; Huang & Zebker, 2022; Wang & Chen, 2022). In areas with severe decorrelation, only phase measurements at PS pixels are suitable for surface deformation analysis. To further advance the capability of PS interferometry, Ferretti et al. (2011) jointly analyzed nearby pixels (Distributed Scatterers) with homogeneous amplitude distributions (referred to as statistically homogeneous pixels or SHP). The InSAR phase observations from each SHP group are averaged to improve the signal-to-noise-ratio (SNR) and a covariance matrix model (Guarnieri & Tebaldini, 2008) is employed to filter phase measurements for surface deformation analysis.

While different selection criteria are adopted in existing PS/DS algorithms, they often require InSAR phase measurements to remain stable at the identified PS/DS over the entire InSAR observation period. However, even at relatively stable PS/DS pixels, phase measurements are often decorrelated in a portion of the interferograms. It is common to assume interferograms with longer temporal baselines tend to decorrelate more than interferograms with shorter temporal baselines. However, other factors (e.g., weather and surface conditions) may cause decorrelation as well. Based on these observations, we design a processing strategy that selects an interferogram subset for surface deformation analysis based on decorrelation and the associated phase unwrapping errors, regardless of interferogram temporal baselines. This new workflow allows us to enhance phase coherence and reduce decorrelation noise through an optional step that integrates recent phase reconstruction algorithms (e.g., Guarnieri & Tebaldini, 2008; Fornaro et al., 2015; Ansari et al., 2018). This InSAR processing strategy is computationally efficient and easy to implement, and can be incorporated into existing workflows to extend the use of the Small BAseline Subset approaches over densely vegetated areas.

2 Methodology

Interferometric Synthetic Aperture Radar (InSAR) techniques compute the phase difference between two SAR images over the same area of interest. After removing the phase component related to surface topography, the observed InSAR phase at a pixel of interest, $\Delta\phi$, can be written as (Hanssen, 2001):

$$\Delta\phi = \frac{4\pi}{\lambda}\Delta d_{LOS} + \Delta\phi_{orb} + \Delta\phi_{decor} + \Delta\phi_{unwrap} + \Delta\phi_{dem} + \Delta\phi_{iono} + \Delta\phi_{tropo} + \Delta\phi_{n} \quad (1)$$

where λ is the radar wavelength and Δd_{LOS} is the surface deformation between two SAR acquisition dates along the radar line-of-sight (LOS) direction. The remaining phase terms on the right are InSAR measurement noise due to orbital errors, phase decorrelation and associated unwrapping errors, digital elevation model (DEM) errors, ionospheric and tropospheric artifacts, and other smaller residual noise terms such as thermal or soil moisture effects. Among these noise terms, orbital errors, DEM errors, and ionospheric delays can be corrected during the interferogram formation (e.g., Fattahi & Amelung, 2013; Fattahi et al., 2017). Additionally, stratified tropospheric noise can be estimated and removed using a combination of global or local atmospheric weather models along with zenith tropospheric delay measurements at GNSS sites (e.g., the GACOS correction as described in Yu et al. (2017)). Therefore, our algorithm design focuses on the reduction of decorrelation and the associated phase unwrapping errors (H. A. Zebker & Villasenor, 1992) as well as tropospheric turbulence noise errors (e.g., H. A. Zebker et al., 1997; Emardson et al., 2003).

Given N high-quality interferograms derived from M SAR acquisitions, Berardino et al. (2002) proposed a method to solve for the surface deformation time series at a pixel of interest as:

$$Bv = \Delta\Phi \tag{2}$$

where $v = [v_1, ..., v_{M-1}]^T$ is the vector of unknown mean velocities between each consecutive SAR acquisition, and $\Delta\Phi = [\Delta\phi_1, ..., \Delta\phi_N]^T$ is a $N\times1$ vector of observed InSAR phases at the given pixel. B is the $N\times(M-1)$ system matrix as defined in (Berardino et al., 2002), and we can solve for v as an inverse problem of Equation (2).

Berardino et al. (2002) named this InSAR time series analysis algorithm the Small BAseline Subset (SBAS) method because a subset of N high-quality InSAR observations is chosen for the time series inversion based on user-defined temporal and spatial baseline thresholds (Fig. 1, left). The algorithm was designed based on the fact that interferograms with large temporal or spatial baselines are more likely to suffer from more severe decorrelation noise. Thus, selecting a subset of interferograms with small baselines allows users to limit the total number of decorrelated phase measurements in the InSAR phase vector Φ in Equation (2). By contrast, tropospheric turbulence noise is not correlated with temporal or spatial baselines (e.g., Tymofyeyeva & Fialko, 2015; M. S. Zebker et al., 2023). Because tropospheric turbulence noise can be considered spatially coherent (similar to deformation signals) but random in time between SAR acquisitions (Emardson et al., 2003), it is desirable to include a large number of interferograms acquired on different dates (especially those with long temporal baselines and thus larger secular deformation signals) as input data for the SBAS inversion (Supporting Information S1).

One limitation of the SBAS approach is that the InSAR decorrelation noise level cannot be measured using temporal and spatial baseline alone. In areas with dense vegetation, a short temporal baseline threshold (e.g., 48 or 60 days) is often imposed to limit temporal decorrelation noise due to vegetation growth in the interferogram subset. However, this leads to a substantial reduction in the total number of phase observations used in time series inversion, which limits our ability to mitigate tropospheric noise (e.g., H. A. Zebker et al., 1997; Zheng et al., 2021) and closure phase biases (e.g., Ansari et al., 2021; Zheng et al., 2022). A small portion of interferograms with longer temporal baselines (e.g., a year) often maintain good phase coherence at certain stable pixels such as roads, man-made structures, and barren terrain. These phase observations can improve the accuracy of the SBAS surface deformation estimates. Based on these facts, our new workflow is designed to choose the interferogram subset based on the phase quality of the interferogram, rather than temporal and spatial baseline thresholds (Fig. 1, right). To do this, we first form all possible interferogram pairs. If severe decorrelation noise is present, we enhance InSAR phase quality through phase reconstruction methods such as coherence-based filtering (e.g., Guarnieri & Tebaldini, 2008; Ferretti et al., 2011; Fornaro et al., 2015; Mirzaee et al., 2023) or an interpolation between phase observations at stable PS pixels (e.g., Ferretti et al., 2000; Hooper et al., 2004; Agram, 2010). This increases the total number of interferograms suitable for the time series analysis. The reconstructed interferograms are then unwrapped. Finally, we compute the amount of unwrapping errors for each interferogram and choose a subset of interferograms with small total phase unwrapping errors as input for the time series inversion. For each unwrapped interferogram, we define the phase unwrapping error at a pixel m as:

$$\phi_m^{err} = \sum_k^4 \Delta\phi_{mn}, \text{ if } \Delta\phi_{mn} > \pi \tag{3}$$

where $\Delta\phi_{mn}$ is the unwrapped phase difference between pixel m and n in an interferogram, and pixel n is one of four adjacent pixels to center pixel m. If $\Delta\phi_{mn} < \pi$, the unwrapping error contribution is 0, as defined in C. Chen and Zebker (2001). We compute the total phase unwrapping error of an interferogram as the sum of the phase unwrapping error over all radar pixels (Wang & Chen, 2022).

3 Test Sites and Data Processing

Our first study site is the Tulare Basin in the southern portion of the Central Valley, California (Fig. S1, left), a large agricultural region that has relied on groundwater since the early 1920s (Poland, 1975). The groundwater demand in combination with extended droughts throughout California has led to aquifer sediment compaction and subsequent land subsidence (e.g., Galloway et al., 1999; Faunt et al., 2016). As a result, InSAR techniques have been used to monitor pumping-induced land subsidence and estimate permanent groundwater loss in the region (e.g., Farr & Liu, 2015; Smith et al., 2017; Ojha et al., 2018; Neely et al., 2021). Our second study site is in Central Texas and contains a portion of the Eagle Ford Shale, southeast of the San Antonio-Austin metroplex (Fig. S1, right). The Eagle Ford Shale is a large oil-producing region. The recent ramp-up in shale fracking activities led to increased reliance on groundwater resources from the Carrizo-Wilcox aquifer that overlays the Eagle Ford Shale (Scanlon et al., 2020). This combination of groundwater withdrawal and oil and gas production can produce complex deformation signals. The growth of vegetation at both of these sites can lead to severe decorrelation in interferograms with relatively short temporal baselines (e.g., $\sim$ 2 months), a challenging scenario for InSAR time series analysis. Furthermore, because both sites are located in the mid-latitude and are relatively flat regions, DEM and ionospheric noise terms are not substantial. Given that the primary noise terms are tropospheric turbulence noise and decorrelation, we chose these two sites to demonstrate the advantages of our time series analysis workflow.

For the California case, we processed 122 C-Band Sentinel-1 SAR images (path 137, frame 114) acquired between 2017 and 2021 using a geocoded single-look-complex (SLC) algorithm (e.g., H. A. Zebker, 2017; Zheng & Zebker, 2017). Because Sentinel-1 satellites have precise orbit controls, the spatial baselines of all interferogram pairs are much smaller than the InSAR critical baseline (Rosen et al., 2000). As a result, we did not observe any noticeable spatial decorrelation artifacts, and our analysis is mainly focused on the mitigation of temporal decorrelation noise. Following the new workflow, we generated all 6498 interferogram pairs without any spatial or temporal thresholds. To enhance the spatial coherence of InSAR phase measurements, we selected PS pixels based on the cosine similarity method (Wang & Chen, 2022), performed a phase interpolation among PS pixels (J. Chen et al., 2015), and unwrapped InSAR phase measurements using the Statistical-Cost, Network-flow Algorithm for Phase Unwrapping (SNAPHU) (C. Chen & Zebker, 2001) algorithm. We solved for the long-term deformation trend over the study period based on a linear deformation (constant velocity) model from interferograms with the phase unwrapping error $<$ 10,000 radians. In a control SBAS experiment, we formed interferogram subsets with various temporal baseline thresholds (e.g., 12, 48, 360, and 1000 days). For example, a 48-day interferogram subset contains all interferograms with $<=$ 48-day temporal baselines. For each small baseline subset, we unwrapped InSAR phase measurements using SNAPHU and solved for the cumulative LOS deformation over the study period based on the same linear deformation (constant velocity) model.

For the Texas case, we followed a similar processing strategy and processed 123 C-band Sentinel-1 images (path 107, frame 92). Using the new workflow, we generated all

7503 interferogram pairs without any spatial or temporal thresholds and improved InSAR phase quality through a PS-interpolation. We solved for the cumulative LOS deformation over the study period based on a linear deformation model using a subset of interferograms with the total phase unwrapping error $<$ 100,000 radians. In a control SBAS experiment, we chose temporal baseline thresholds of 12, 24, 48, 96, and 180 days to form small baseline interferogram subsets. For each small baseline subset, we unwrapped InSAR phase measurements and solved for the cumulative LOS deformation over the study period based on the same linear deformation model.

There are 25 permanent GPS stations with continuous records between 2017 and 2021 over the Tulare Basin (Fig. S1, left). Because InSAR techniques only measure relative deformation with respect to a reference pixel, we chose the GPS station P544 as the reference point to calibrate and used the remaining 24 GPS stations as controls to validate InSAR results. We projected the GPS daily East, North, and Up (ENU) time series (independently processed by the Nevada Geodetic Laboratory) to the radar LOS direction and estimated the average surface deformation rate in mm/year from both GPS and InSAR observations. We used the InSAR and GPS rate misfit, Δ_v to quantify the uncertainty in InSAR surface deformation solutions derived from different subsets. Similarly, we chose the GPS station TXFL as the reference point for the Texas case and used the remaining 5 stations as independent controls to validate InSAR results (Fig. S1, right).

4 Results and Discussion

4.1 The relationship between phase quality and temporal baselines

The Tulare Basin and Eagle Ford sites are covered with dense vegetation and the vegetation growth between radar acquisitions causes severe decorrelation, which appears random in space (e.g., Fig. 2 columns a and c). The InSAR phase measurement at a severely decorrelated radar pixel can be considered a random wrapped phase value between 0 and 2π, and no longer contains spatially coherent phase information such as surface deformation signals or tropospheric noise. Unwrapping interferograms with severe decorrelation artifacts is time-consuming and unreliable, and often introduces large phase unwrapping errors that dominate in the final InSAR time series solutions. We emphasize that not all radar pixels decorrelate at the same rate. For example, roads, buildings, and rock outcrops can remain coherent over a much longer period of time than agricultural field pixels. Therefore, we identified phase measurements at relatively stable PS pixels and interpolated between PS pixels to improve InSAR spatial phase coherence (e.g., Fig. 2 columns b and d) and reduced unwrapping time (Table S1).

An important finding of this study is that temporal baseline is not always a robust measure for selecting the interferogram subset (Fig. 2). For the Texas case, some reconstructed interferograms with longer temporal baselines (e.g., over 400 days) contain smaller phase unwrapping errors than those with shorter temporal baselines (e.g., 60 days). We found that interferograms formed from winter SAR scenes often have better phase coherence than interferograms formed from summer SAR scenes. This is because after deciduous trees lose their leaves in the fall, radar signals reflected from tree trunks can maintain coherence over a long period of time. Furthermore, some radar images contain large tropospheric noise anomalies due to heat waves or tropical storms (Staniewicz et al., 2020). Interferograms formed using these radar images tend to suffer from severe decorrelation noise regardless of temporal baselines. In summary, we identified a total of 2360 (out of 7503) interferograms with phase unwrapping errors $<$ 100,000 radians for the Texas case. Among these interferograms, there are 865 that span $>$200 days and 188 interferograms that span $>$1 year. For the California case, we identified a total of 527 (out of 6389) interferograms with phase unwrapping errors $<$ 10,000 radians. Among those interferograms, 127 interferograms span $>$60 days and 7 span $>$90 days. We imposed a smaller total phase unwrapping error threshold for the California case because: (1) while dense vegetation is only present over a portion of the Tulare Basin site covered with agricultural fields, it is present over the entire Eagle Ford site (Fig. S1). Therefore, the total phase unwrapping error is smaller in the Tulare Basin interferograms than in the Eagle Ford interferograms when similar decorrelation artifacts occur; and (2) the expected subsidence trend is much larger at the Tulare Basin site than the Eagle Ford site. Fewer interferograms are required to reduce tropospheric noise in order to reconstruct a larger deformation signal. In addition, interferograms with large deformation signals (e.g. Tulare Basin interferograms with long temporal baselines) may be prone to aliasing because the density of high-quality InSAR pixels is too low to capture the rapidly changing InSAR fringes (Pepin & Zebker, 2024).

4.2 The Tulare Basin results

The Tulare Basin LOS deformation estimates derived from a subset of interferograms with small phase unwrapping errors show up to 150 mm/yr LOS deformation (Fig. 3a) with a mean absolute error (MAE) of 3.4 mm/yr and a maximum absolute error of 9.1 mm/yr based on independent GPS validation (Fig. 3g and Table S2). The observed deformation pattern is geographically consistent with recent InSAR studies (e.g., Farr, 2018; Murray & Lohman, 2018; Ojha et al., 2019; Neely et al., 2021; Kang & Knight, 2023). For example, Neely et al. (2021) analyzed 263 Sentinel-1 interferograms (with temporal baselines < 100 days) and observed up to ~ 270 mm/yr subsidence between April 2015 and October 2017. The average velocity residual was 2.9 mm/yr based on independent GPS validation. They found that the subsidence rate changes throughout the year in response to water demand. Up to 345 mm/yr vertical subsidence (with an average velocity residual of 6.4 mm/yr) was observed during the dry period of October 2015 - September 2016, while up to 177 mm/yr vertical subsidence (with an average velocity residual of 11.1 mm/yr) was observed during the wet period of October 2016 - September 2017. Ojha et al. (2019) and Kang and Knight (2023) reported similar error residuals but different rate magnitudes, likely due to differences in the study period and InSAR processing methodologies.

To further illustrate how the InSAR processing strategy may influence SBAS solutions, Fig. 3b-f shows the LOS surface deformation rate estimates derived from different small baseline subsets. The deformation solution derived from the 12-day interferogram subset (denoted as "SBAS-12') shows an MAE of 13.9 mm/yr and a maximum absolute error of 29.2 mm/yr (Fig. 3g and Table S2). Given that we observed minimal decorrelation artifacts (thus minimal phase unwrapping errors) in 12-day interferograms, the errors in the SBAS-12 solution are primarily due to tropospheric noise. The SBAS-48 solution shows an MAE of 3.7 mm/yr and a maximum absolute error of 9.7 mm/yr, which is comparable to the deformation solution derived from the interferogram subset with small phase unwrapping errors. We again observed minimal decorrelation artifacts in the SBAS-48 interferogram subset, and tropospheric noise is the primary error source. In this case, interferograms with longer temporal baselines contain larger secular deformation signals than interferograms with shorter temporal baselines, while the tropospheric noise level among these interferograms is similar. As a result, the inclusion of interferograms with longer temporal baselines can better reduce the residual tropospheric noise level in the SBAS deformation rate estimates (Supporting Information S1). However, the deformation solutions derived from a subset of interferograms with temporal baselines up to 180, 360, and 1000 days have an increasing MAE of 4.3, 5.2, and 11.5 mm/yr. This is because decorrelation artifacts are observed in interferograms with temporal baselines ~ 2 months and longer. As the temporal baseline threshold increases, more decorrelated InSAR phase observations are used in the SBAS inversion. In particular, most of the interferograms in the SBAS-1000 subset are completely decorrelated over the agricultural fields. As a result, fitting a linear deformation model to decorrelated InSAR observations may yield a near-zero deformation rate estimate when the number of decorrelated observations is sufficiently large. A systematic underestimation (up to 55.2 mm/yr) was observed in the SBAS-1000 solution at all GPS stations where a non-trivial deformation signal is present (Fig. 3g and Table S2). We emphasize it is important to evaluate the accuracy of InSAR deformation estimates at GPS stations where non-trivial deformation is present. Because a large number of random decorrelated InSAR observations may yield near-zero deformation rate estimates, they often appear to be "consistent" with GPS observations at relatively stable locations. However, this does not mean decorrelated InSAR measurements contain any information about the true deformation signals, and they should be excluded in the SBAS inversion.

4.3 The Eagle Ford region results

The Eagle Ford LOS deformation estimates derived from a subset of interferograms with small phase unwrapping error reveals a $\sim$900 km^2 region of up to 11 cm of cumulative LOS deformation between February 2017 and December 2021 (Fig. 4a). The MAE at 5 GPS permanent stations is 2.7 mm/year and a maximum absolute error is 4.8 mm/year at TXCU (Fig. 4a and Table S3). The observed subsidence signal (Fig. 4a) aligns well with oil and gas production wells (The Railroad Commission of Texas, 2023). This region experienced a ramp-up in oil and gas production around 2010. Approximately 20-25 million barrels of oil (bbl) and 100-120 million one thousand cubic feet (mcf) of gas were produced every month since 2014 (The Railroad Commission of Texas, 2023). Similarly, comparable volumes of subsurface water are co-produced with oil and gas. Approximately 1246 million bbl of water from unconventional wells was produced from 2009-2016 in the Eagle Ford with 337, 291, and 206 million bbl of produced water each year for 2014, 2015, and 2016 respectively (Scanlon et al., 2019). Here, it is likely that the production of water, oil, and gas all contribute to the observed land subsidence (Fig. S2).

In contrast, the LOS surface deformation rate estimates derived from different small baseline subsets failed to detect this large deformation signal (Fig. 4b-f). The SBAS solution derived from the 12-day interferogram subset (Fig. 4b) has an MAE of 5.5 mm/yr and a maximum absolute error of 16 mm/yr. Given that we observed minimal decorrelation artifacts in the 12-day interferograms (e.g., Fig. S3a and g), the residuals are mostly due to tropospheric noise. We note that there are only five GPS validation stations over the Eagle Ford region. As a result, the GPS-InSAR misfit only represents the InSAR measurement accuracy at these five locations (Table S3), and InSAR noise residuals can be much larger over regions with visible tropospheric noise artifacts. Because the study site is densely vegetated, we observed decorrelation artifacts and associated phase unwrapping errors even in some 24-day interferograms (Fig. S3h). As a result, both tropospheric noise and decorrelation artifacts are present in the SBAS-24 solution, and decorrelation-related artifacts dominate in the SBAS-48, SBAS-96, and SBAS-180 solutions. While unwrapping errors often lead to a systematic underestimation of the true deformation rate (e.g., in the Tulare Basin case Fig. 3f), decorrelation signatures can sometimes be unpredictable. In the Eagle Ford case, very large phase unwrapping errors are present in a subset of interferograms, which produced unrealistic artifacts in the SBAS-48, SBAS-96, and SBAS-180 solutions. We emphasize that it is important to employ a phase reconstruction technique to enhance phase quality prior to the surface deformation analysis over densely vegetated areas such as the Eagle Ford region. However, some long temporal baseline interferograms are reconstructed successfully, while some short temporal baseline interferograms fail to be reconstructed (Fig. 2). Therefore, selecting interferograms based on an unwrapping error threshold is more robust than a temporal baseline threshold over regions with large tropospheric noise and severe decorrelation artifacts.

While there are numerous InSAR surface deformation studies over the less vegetated Permian Basin in West Texas (Kim & Lu, 2018; Staniewicz et al., 2020; Zhai et al., 2021; Hennings et al., 2021; Pepin et al., 2022), our study is the first that observes a large subsidence feature with spatially dense information over the Eagle Ford region in Central Texas. Surface deformation can be used to derive subsurface stress and pore pressure changes related to oil and gas injection and extraction (e.g., Yang et al., 2015; Vasco et al., 2016; Shirzaei et al., 2019; Deng et al., 2020). These changes in the subsurface can eventually result in fault slip and trigger earthquakes (Segall, 1989). For example, Frohlich and Brunt (2013) reported 62 earthquakes in the Eagle Ford region from 2009-2011, highlighted by a M_w 4.8 earthquake in October 2011 in Fashing, TX. They found that most of the seismicity followed fluid extraction, not injection. Recently, the Eagle Ford region has experienced a noticeable increase in seismic activity, and there were 165, 341, 336, 349 earthquakes recorded in 2017-2018, 2019-2020, 2021-2022, 2023-March 13, 2024, respectively (Fig. 4a) (TexNet, 2024). In particular, two earthquakes (M_L 4.3 and M_L 4.7) occurred on February 17, 2024 near Falls City, which were felt by many San Antonio and Austin residents. The increase in magnitude and frequency of these large seismic events requires further scientific investigation, and InSAR data can play an important role in these future induced seismicity studies.

5 Conclusion

In this study, we found that selecting an interferogram subset based on phase quality rather than temporal baseline leads to better mitigation of decorrelation and tropospheric noise. In the Tulare Basin case, our InSAR processing strategy generated a deformation solution comparable to the SBAS solution when the optimal temporal baseline threshold was employed. In the Eagle Ford case, our processing strategy revealed a large subsidence signature associated with oil and gas operations that is otherwise undetectable due to the presence of large tropospheric noise and severe decorrelation artifacts. Our workflow is easy to implement, which can extend the use of the SBAS algorithm over humid and densely vegetated terrain that is challenging for InSAR studies.

6 Open Research

Sentinel-1 SAR imagery over the Tulare Basin, CA (path 137, frame 114) and Eagle Ford region, TX (path 107, frame 92) can be queried and downloaded from the Alaska Satellite Facility at https://search.asf.alaska.edu. Interferograms with comparable quality can be produced using InSAR processing packages such as the InSAR Scientific Computing Environment 3 (ISCE3) (Rosen et al., 2018), GMTSAR (Sandwell et al., 2011), or GAMMA (Wegmüller et al., 2016). GPS data were processed by the Nevada Geodetic Laboratory and downloaded at http://geodesy.unr.edu/NGLStationPages/GlobalStationList (Blewitt et al., 2018). A list of available GPS stations over the Tulare Basin and the Eagle Ford region can be found in the Supporting Information.

Acknowledgments

This research was funded by the NASA Earth Surface and Interior Program grant numbers 80NSSC18K0467 and 80NSSC22K0412.

References

Agram, P. (2010, 01). Persistent scatterer interferometry in natural terrain.

Amelung, F., Galloway, D. L., Bell, J. W., Zebker, H. A., & Laczniak, R. J. (1999, 06). Sensing the ups and downs of Las Vegas: InSAR reveals structural control of land subsidence and aquifer-system deformation. *Geology*, *27*(6), 483-486. Retrieved from `https://doi.org/10.1130/0091-7613(1999)027<0483:STUADO>2.3.CO;2` doi: 10.1130/0091-7613(1999)027⟨0483:STUADO⟩2.3.CO;2

Ansari, H., De Zan, F., & Bamler, R. (2018). Efficient phase estimation for interferogram stacks. *IEEE Transactions on Geoscience and Remote Sensing*, *56*(7), 4109-4125. doi: 10.1109/TGRS.2018.2826045

Ansari, H., De Zan, F., & Parizzi, A. (2021). Study of systematic bias in measuring surface deformation with SAR interferometry. *IEEE Transactions on Geoscience and Remote Sensing*, *59*(2), 1285-1301. doi: 10.1109/TGRS.2020.3003421

Bekaert, D., Hooper, A., & Wright, T. J. (2015a). A spatially variable power law tropospheric correction technique for InSAR data. *Journal of Geophysical Research: Solid Earth*, *120*(2), 1345-1356. Retrieved from `https://agupubs.onlinelibrary.wiley.com/doi/abs/10.1002/2014JB011558` doi: https://doi.org/10.1002/2014JB011558

Bekaert, D., Walters, R., Wright, T., Hooper, A., & Parker, D. (2015b, 09). Statistical comparison of InSAR tropospheric correction techniques. *Remote Sensing of Environment*, *170*, 40–47. doi: 10.1016/j.rse.2015.08.035

Bell, J., Amelung, F., Ferretti, A., Bianchi, M., & Novali, F. (2008, 02). Permanent scatterer InSAR reveals seasonal and long-term aquifer-system response to groundwater pumping and artificial recharge. *Water Resources Research*, *44*. doi: 10.1029/2007WR006152

Berardino, P., Fornaro, G., Lanari, R., & Sansosti, E. (2002). A new algorithm for surface deformation monitoring based on small baseline differential SAR interferograms. *IEEE Transactions on Geoscience and Remote Sensing*, *40*(11), 2375-2383. doi: 10.1109/TGRS.2002.803792

Bevis, M., Businger, S., Herring, T. A., Rocken, C., Anthes, R. A., & Ware, R. H. (1992). GPS meteorology: Remote sensing of atmospheric water vapor using the global positioning system. *Journal of Geophysical Research: Atmospheres*, *97*(D14), 15787-15801. Retrieved from `https://agupubs.onlinelibrary.wiley.com/doi/abs/10.1029/92JD01517` doi: https://doi.org/10.1029/92JD01517

Blewitt, G., Hammond, W. C., & Kreemer, C. (2018). Harnessing the GPS data explosion for interdisciplinary science. *EOS*, *99*. doi: https://doi.org/10.1029/2018EO104623

Chaussard, E., Bürgmann, R., Shirzaei, M., Fielding, E. J., & Baker, B. (2014). Predictability of hydraulic head changes and characterization of aquifer-system and fault properties from InSAR-derived ground deformation. *Journal of Geophysical Research: Solid Earth*, *119*(8), 6572-6590. Retrieved from `https://agupubs.onlinelibrary.wiley.com/doi/abs/10.1002/2014JB011266` doi: https://doi.org/10.1002/2014JB011266

Chen, C., & Zebker, H. (2001, 03). Two-dimensional phase unwrapping with use of statistical models for cost functions in nonlinear optimization. *Journal of the Optical Society of America. A, Optics, image science, and vision*, *18*, 338-51. doi: 10.1364/JOSAA.18.000338

Chen, J., Zebker, H. A., & Knight, R. (2015). A persistent scatterer interpolation for retrieving accurate ground deformation over InSAR-decorrelated agricultural fields. *Geophysical Research Letters*, *42*(21), 9294-9301. Retrieved from `https://agupubs.onlinelibrary.wiley.com/doi/abs/10.1002/2015GL065031` doi: https://doi.org/10.1002/2015GL065031

Deng, F., Dixon, T. H., & Xie, S. (2020). Surface deformation and induced seismicity due to fluid injection and oil and gas extraction in Western Texas. *Journal of Geophysical Research: Solid Earth*, *125*(5), e2019JB018962. Retrieved from `https://agupubs.onlinelibrary.wiley.com/doi/abs/10.1029/2019JB018962` (e2019JB018962 2019JB018962) doi: https://doi.org/10.1029/2019JB018962

Doin, M., Lasserre, C., Peltzer, G., Cavalié, O., & Doubre, C. (2009). Corrections of stratified tropospheric delays in SAR interferometry: Validation with global atmospheric models. *Journal of Applied Geophysics*, *69*(1), 35-50.

Retrieved from https://www.sciencedirect.com/science/article/pii/S0926985109000603 (Advances in SAR Interferometry from the 2007 Fringe Workshop) doi: https://doi.org/10.1016/j.jappgeo.2009.03.010

Emardson, T., Simons, M., & Webb, F. (2003, 05). Neural atmospheric delay in interferometric Synthetic Aperture Radar applications: statistical description and mitigation. *Journal of Geophysical Research*, *108*. doi: 10.1029/2002JB001781

Farr, T. G. (2018). InSAR measurements of subsidence and rebound in California. In *IGARSS 2018 - 2018 IEEE International Geoscience and Remote Sensing Symposium* (p. 8401-8403). IEEE.

Farr, T. G., & Liu, Z. (2015). Monitoring subsidence associated with ground water dynamics in the Central Valley of California using interferometric radar. *Geophysical Monograph*, *206*, 397-406.

Fattahi, H., & Amelung, F. (2013). DEM error correction in InSAR time series. *IEEE Transactions on Geoscience and Remote Sensing*, *51*(7), 4249-4259. doi: 10.1109/TGRS.2012.2227761

Fattahi, H., Simons, M., & Agram, P. (2017). InSAR time-series estimation of the ionospheric phase delay: An extension of the split range-spectrum technique. *IEEE Transactions on Geoscience and Remote Sensing*, *55*(10), 5984-5996. doi: 10.1109/TGRS.2017.2718566

Faunt, C. C., Sneed, M., Traum, J., & Brandt, J. T. (2016). Water availability and land subsidence in the Central Valley, California, USA. *Hydrogeology journal*, *24*(3), 675-684.

Ferretti, A., Fumagalli, A., Novali, F., Prati, C., Rocca, F., & Rucci, A. (2011). A new algorithm for processing interferometric data-stacks: SqueeSAR. *IEEE Transactions on Geoscience and Remote Sensing*, *49*(9), 3460-3470. doi: 10.1109/TGRS.2011.2124465

Ferretti, A., Prati, C., & Rocca, F. (2000). Nonlinear subsidence rate estimation using permanent scatterers in differential SAR interferometry. *IEEE Transactions on Geoscience and Remote Sensing*, *38*(5), 2202-2212. doi: 10.1109/36.868878

Fialko, Y., Sandwell, D., Agnew, D., Simons, M., Shearer, P., & Minster, B. (2002). Deformation on nearby faults induced by the 1999 Hector Mine earthquake. *Science*, *297*(5588), 1858-1862. Retrieved from https://www.science.org/doi/abs/10.1126/science.1074671 doi: 10.1126/science.1074671

Fielding, E., Sangha, S., Bekaert, D., Samsonov, S., & Chang, J. (2017, 07). Surface deformation of North-Central Oklahoma related to the 2016 Mw 5.8 Pawnee earthquake from SAR interferometry time series. *Seismological Research Letters*, *88*, 971-982. doi: 10.1785/0220170010

Fornaro, G., Verde, S., Reale, D., & Pauciullo, A. (2015). CAESAR: An approach based on covariance matrix decomposition to improve multibaseline–multitemporal interferometric SAR processing. *IEEE Transactions on Geoscience and Remote Sensing*, *53*(4), 2050-2065. doi: 10.1109/TGRS.2014.2352853

Frohlich, C., & Brunt, M. (2013). Two-year survey of earthquakes and injection/production wells in the Eagle Ford Shale, Texas, prior to the MW4.8 20 October 2011 earthquake. *Earth and Planetary Science Letters*, *379*, 56-63. Retrieved from https://www.sciencedirect.com/science/article/pii/S0012821X13004007 doi: https://doi.org/10.1016/j.epsl.2013.07.025

Galloway, D. L., Jones, D. R. D. R., & Ingebritsen, S. E. (1999). *Land subsidence in the United States / edited by Devin Galloway, David R. Jones, S.E. Ingebritsen.* Reston, VA: U.S. Geological Survey.

Guarnieri, A. M., & Tebaldini, S. (2008). On the exploitation of target statistics for SAR interferometry applications. *IEEE Transactions on Geoscience and Remote Sensing*, *46*(11), 3436-3443. doi: 10.1109/TGRS.2008.2001756

Hanssen, R. (2001). *Radar interferometry: Data interpretation and error analysis.* Springer.

Hennings, P., Dvory, N., Horne, E., Li, P., Savvaidis, A., & Zoback, M. (2021, 08). Stability of the Fault Systems That Host-Induced Earthquakes in the Delaware Basin of West Texas and Southeast New Mexico. *The Seismic Record*, *1*(2), 96-106. Retrieved from https://doi.org/10.1785/0320210020 doi: 10.1785/0320210020

Hoffmann, J., Zebker, H., Galloway, D., & Amelung, F. (2001, 06). Seasonal subsidence and rebound in Las Vegas Valley, Nevada, observed by Synthetic Aperture Radar Interferometry. *Water Resources Research*, *37*, 1551-1566. doi: 10.1029/2000WR900404

Hooper, A., Zebker, H., Segall, P., & Kampes, B. (2004). A new method for measuring deformation on volcanoes and other natural terrains using InSAR persistent scatterers. *Geophysical Research Letters*, *31*(23). Retrieved from https://agupubs.onlinelibrary.wiley.com/doi/abs/10.1029/2004GL021737 doi: https://doi.org/10.1029/2004GL021737

Huang, S. A., & Zebker, H. A. (2022). InSAR time-series analysis with a non-Gaussian detector for persistent scatterers. *IEEE Journal of Selected Topics in Applied Earth Observations and Remote Sensing*, *15*, 9208-9225. doi: 10.1109/JSTARS.2022.3216964

Jolivet, R., Grandin, R., Lasserre, C., Doin, M.-P., & Peltzer, G. (2011). Systematic InSAR tropospheric phase delay corrections from global meteorological reanalysis data. *Geophysical Research Letters*, *38*(17). Retrieved from https://agupubs.onlinelibrary.wiley.com/doi/abs/10.1029/2011GL048757 doi: https://doi.org/10.1029/2011GL048757

Jónsson, S., Amelung, F., Zebker, H., & Segall, P. (2000). Widespread uplift and 'trapdoor' faulting on galápagos volcanoes observed with radar interferometry. *Nature (London)*, *407*(6807), 993-996.

Kang, S., & Knight, R. (2023). Isolating the poroelastic response of the groundwater system in InSAR data from the Central Valley of California. *Geophysical Research Letters*, *50*(9), e2023GL103222. Retrieved from https://agupubs.onlinelibrary.wiley.com/doi/abs/10.1029/2023GL103222 (e2023GL103222 2023GL103222) doi: https://doi.org/10.1029/2023GL103222

Kim, J.-W., & Lu, Z. (2018, 03). Association between localized geohazards in West Texas and human activities, recognized by Sentinel-1A/B satellite radar imagery. *Scientific Reports*, *8*. doi: 10.1038/s41598-018-23143-6

Li, Z., Fielding, E. J., Cross, P., & Preusker, R. (2009). Advanced InSAR atmospheric correction: MERIS/MODIS combination and stacked water vapour models. *International Journal of Remote Sensing*, *30*(13), 3343-3363. Retrieved from https://doi.org/10.1080/01431160802562172 doi: 10.1080/01431160802562172

Lundgren, P., Poland, M., Miklius, A., Orr, T., Yun, S.-H., Fielding, E., ... Owen, S. (2013). Evolution of dike opening during the march 2011 kamoamoa fissure eruption, kīlauea volcano, hawai'i. *Journal of Geophysical Research: Solid Earth*, *118*(3), 897-914. Retrieved from https://agupubs.onlinelibrary.wiley.com/doi/abs/10.1002/jgrb.50108 doi: https://doi.org/10.1002/jgrb.50108

McKeighan, C., Hennings, P., Horne, E. A., Smye, K., & Morris, A. (2022, 10). Understanding Anthropogenic Fault Rupture in the Eagle Ford Region, South-Central Texas. *Bulletin of the Seismological Society of America*, *112*(6), 2870-2889. Retrieved from https://doi.org/10.1785/0120220074 doi: 10.1785/0120220074

Mirzaee, S., Amelung, F., & Fattahi, H. (2023). Non-linear phase linking using joined distributed and persistent scatterers. *Computers Geosciences*, *171*, 105291. Retrieved from https://www.sciencedirect.com/science/article/

pii/S0098300422002400 doi: https://doi.org/10.1016/j.cageo.2022.105291

Murray, K. D., & Lohman, R. B. (2018). Short-lived pause in Central California subsidence after heavy winter precipitation of 2017. *Science Advances*, *4*(8), eaar8144. Retrieved from https://www.science.org/doi/abs/10.1126/sciadv.aar8144 doi: 10.1126/sciadv.aar8144

Neely, W. R., Borsa, A. A., Burney, J. A., Levy, M. C., Silverii, F., & Sneed, M. (2021). Characterization of groundwater recharge and flow in California's San Joaquin Valley from InSAR-observed surface deformation. *Water resources research*, *57*(4), e2020WR028451-n/a.

Ojha, C., Shirzaei, M., Werth, S., Argus, D. F., & Farr, T. G. (2018). Sustained groundwater loss in California's Central Valley exacerbated by intense drought periods. *Water Resources Research*, *54*(7), 4449-4460. Retrieved from https://agupubs.onlinelibrary.wiley.com/doi/abs/10.1029/2017WR022250 doi: https://doi.org/10.1029/2017WR022250

Ojha, C., Werth, S., & Shirzaei, M. (2019). Groundwater loss and aquifer system compaction in San Joaquin Valley during 2012–2015 drought. *Journal of Geophysical Research: Solid Earth*, *124*(3), 3127-3143. Retrieved from https://agupubs.onlinelibrary.wiley.com/doi/abs/10.1029/2018JB016083 doi: https://doi.org/10.1029/2018JB016083

Pepin, K., Ellsworth, W., Sheng, Y., & Zebker, H. (2022, 02). Shallow aseismic slip in the Delaware Basin determined by Sentinel-1 InSAR. *Journal of Geophysical Research: Solid Earth*, *127*. doi: 10.1029/2021JB023157

Pepin, K., & Zebker, H. (2024). Aliasing in InSAR 2d phase unwrapping and time series. *IEEE Transactions on Geoscience and Remote Sensing*, 1-1. doi: 10.1109/TGRS.2024.3359482

Poland, J. F. J. F. (1975). *Land subsidence, in the San Joaquin Valley, California, as of 1972 / by J. F. Poland [and three others]; prepared in cooperation with the California Department of Water Resources.* Washington: United States Department of the Interior, Geological Survey.

Pritchard, M., & Simons, M. (2002, 08). A satellite geodetic survey of large scale deformation of volcanic centers in the Central Andes. *Nature*, *418*, 167-71. doi: 10.1038/nature00872

Rosen, P., Gurrola, E. M., Agram, P., Cohen, J., Lavalle, M., Riel, B. V., ... Buckley, S. M. (2018). The insar scientific computing environment 3.0: A flexible framework for nisar operational and user-led science processing. In *Igarss 2018 - 2018 ieee international geoscience and remote sensing symposium* (p. 4897-4900). doi: 10.1109/IGARSS.2018.8517504

Rosen, P., Hensley, S., Joughin, I., Li, F., Madsen, S., Rodriguez, E., & Goldstein, R. (2000, 04). Synthetic aperture radar interferometry. *Proceedings of the IEEE*, *88*, 333 - 382. doi: 10.1109/5.838084

Sandwell, D., Mellors, R., Tong, X., Wei, M., & Wessel, P. (2011). Gmtsar: An insar processing system based on generic mapping tools.

Scanlon, B., Ikonnikova, S., Qian, Y., & Reedy, R. (2020, 02). Will water issues constrain oil and gas production in the U.S.? *Environmental Science Technology*, *54*, 3510–3519. doi: 10.1021/acs.est.9b06390

Scanlon, B., Weingarten, M., Murray, K., & Reedy, R. (2019). Managing basin-scale fluid budgets to reduce injection-induced seismicity from the recent u.s. shale oil revolution. *Seismological research letters*, *90*(1), 171-182.

Schmidt, D., & Burgmann, R. (2003, 09). Time-dependent land uplift and subsidence in the Santa Clara valley, California, from a large interferometric synthetic aperture radar data set. *Journal of Geophysical Research*, *108*. doi: 10.1029/2002JB002267

Segall, P. (1989). Earthquakes triggered by fluid extraction. *Geology*, *17*(10), 942-946. Retrieved from https://doi.org/10.1130/0091-7613(1989)017<0942:ETBFE>2.3.CO;2 doi: 10.1130/0091-7613(1989)017⟨0942:ETBFE⟩2.3.CO;2

Shirzaei, M., & Bürgmann, R. (2013). Time-dependent model of creep on the Hayward fault from joint inversion of 18 years of InSAR and surface creep data. *Journal of Geophysical Research: Solid Earth*, *118*(4), 1733-1746. Retrieved from https://agupubs.onlinelibrary.wiley.com/doi/abs/10.1002/jgrb.50149 doi: https://doi.org/10.1002/jgrb.50149

Shirzaei, M., Manga, M., & Zhai, G. (2019). Hydraulic properties of injection formations constrained by surface deformation. *Earth and Planetary Science Letters*, *515*, 125-134. Retrieved from https://www.sciencedirect.com/science/article/pii/S0012821X19301736 doi: https://doi.org/10.1016/j.epsl.2019.03.025

Smith, R. G., Knight, R., Chen, J., Reeves, J. A., Zebker, H. A., Farr, T., & Liu, Z. (2017). Estimating the permanent loss of groundwater storage in the southern San Joaquin Valley, California. *Water Resources Research*, *53*(3), 2133-2148. Retrieved from https://agupubs.onlinelibrary.wiley.com/doi/abs/10.1002/2016WR019861 doi: https://doi.org/10.1002/2016WR019861

Staniewicz, S., Chen, J., Lee, H., Olson, J., Savvaidis, A., Reedy, R., ... Hennings, P. (2020). InSAR reveals complex surface deformation patterns over an 80,000km2 oil-producing region in the Permian Basin. *Geophysical Research Letters*, *47*(21), e2020GL090151. Retrieved from https://agupubs.onlinelibrary.wiley.com/doi/abs/10.1029/2020GL090151 (e2020GL090151 10.1029/2020GL090151) doi: https://doi.org/10.1029/2020GL090151

TexNet. (2024). *TexNet High Resolution Earthquake Catalog: Bureau for Economic Geology at University of Texas at Austin.* Retrieved 2024-03-28, from https://doi.org/10.15781/76hj-ed46

The Railroad Commission of Texas. (2023). *Eagle Ford Shale.* Retrieved 2024-03-28, from https://www.rrc.texas.gov/oil-and-gas/major-oil-and-gas-formations/eagle-ford-shale/

Tymofyeyeva, E., & Fialko, Y. (2015). Mitigation of atmospheric phase delays in InSAR data, with application to the eastern California shear zone. *Journal of Geophysical Research: Solid Earth*, *120*(8), 5952-5963. Retrieved from https://agupubs.onlinelibrary.wiley.com/doi/abs/10.1002/2015JB011886 doi: https://doi.org/10.1002/2015JB011886

Vasco, D., Harness, P., Pride, S., & Hoversten, M. (2016, 12). Estimating fluid-induced stress change from observed deformation. *Geophysical Journal International*, *208*(3), 1623-1642. Retrieved from https://doi.org/10.1093/gji/ggw472 doi: 10.1093/gji/ggw472

Wadge, G., Webley, P. W., James, I. N., Bingley, R., Dodson, A., Waugh, S., ... Clarke, P. J. (2002). Atmospheric models, GPS and InSAR measurements of the tropospheric water vapour field over Mount Etna. *Geophysical Research Letters*, *29*(19), 11-1-11-4. Retrieved from https://agupubs.onlinelibrary.wiley.com/doi/abs/10.1029/2002GL015159 doi: https://doi.org/10.1029/2002GL015159

Wang, K., & Chen, J. (2022). Accurate persistent scatterer identification based on phase similarity of radar pixels. *IEEE Transactions on Geoscience and Remote Sensing*, *60*, 1-13. doi: 10.1109/TGRS.2022.3210868

Wegmüller, U., Werner, C., Strozzi, T., Wiesmann, A., Frey, O., & Santoro, M. (2016). Sentinel-1 support in the gamma software. *Procedia Computer Science*, *100*, 1305-1312. Retrieved from https://www.sciencedirect.com/science/article/pii/S1877050916324152 (International Conference on ENTERprise Information Systems/International Conference on Project MANagement/International Conference on Health and Social Care Information Systems and Technologies, CENTERIS/ProjMAN / HCist 2016) doi: https://doi.org/10.1016/j.procs.2016.09.246

Wright, T. J., Parsons, B., England, P. C., & Fielding, E. J. (2004). Insar observations of low slip rates on the major faults of western tibet. *Science*, *305*(5681), 236-239. Retrieved from `https://www.science.org/doi/abs/10.1126/science.1096388` doi: 10.1126/science.1096388

Xu, X., Sandwell, D. T., Klein, E., & Bock, Y. (2021). Integrated Sentinel-1 InSAR and GNSS time-series along the San Andreas fault system. *Journal of Geophysical Research: Solid Earth*, *126*(11), e2021JB022579. Retrieved from `https://agupubs.onlinelibrary.wiley.com/doi/abs/10.1029/2021JB022579` (e2021JB022579 2021JB022579) doi: https://doi.org/10.1029/2021JB022579

Yang, Q., Zhao, W., Dixon, T., Amelung, F., Han, W., & Li, P. (2015, October 1). InSAR monitoring of ground deformation due to CO2 injection at an enhanced oil recovery site, West Texas. *International Journal of Greenhouse Gas Control*, *41*, 20–28. (Publisher Copyright: © 2015 Elsevier Ltd.) doi: 10.1016/j.ijggc.2015.06.016

Yu, C., Penna, N. T., & Li, Z. (2017). Generation of real-time mode high-resolution water vapor fields from GPS observations. *Journal of Geophysical Research: Atmospheres*, *122*(3), 2008-2025. Retrieved from `https://agupubs.onlinelibrary.wiley.com/doi/abs/10.1002/2016JD025753` doi: https://doi.org/10.1002/2016JD025753

Zebker, H. A. (2017). User-friendly insar data products: Fast and simple timeseries processing. *IEEE Geoscience and Remote Sensing Letters*, *14*, 2122-2126.

Zebker, H. A., Rosen, P. A., & Hensley, S. (1997). Atmospheric effects in interferometric synthetic aperture radar surface deformation and topographic maps. *Journal of Geophysical Research: Solid Earth*, *102*(B4), 7547-7563. Retrieved from `https://agupubs.onlinelibrary.wiley.com/doi/abs/10.1029/96JB03804` doi: https://doi.org/10.1029/96JB03804

Zebker, H. A., & Villasenor, J. (1992). Decorrelation in interferometric radar echoes. *IEEE Transactions on Geoscience and Remote Sensing*, *30*(5), 950-959. doi: 10.1109/36.175330

Zebker, M. S., Chen, J., & Hesse, M. A. (2023). Robust surface deformation and tropospheric noise characterization from common-reference interferogram subsets. *IEEE Transactions on Geoscience and Remote Sensing*, *61*, 1-14. doi: 10.1109/TGRS.2023.3288019

Zhai, G., Shirzaei, M., & Manga, M. (2021, 05). Widespread deep seismicity in the Delaware Basin, Texas, is mainly driven by shallow wastewater injection. *Proceedings of the National Academy of Sciences*, *118*, e2102338118. doi: 10.1073/pnas.2102338118

Zheng, Y., Fattahi, H., Agram, P., Simons, M., & Rosen, P. (2022). On closure phase and systematic bias in multilooked SAR interferometry. *IEEE transactions on geoscience and remote sensing*, *60*, 1-11.

Zheng, Y., Zebker, H., & Michaelides, R. (2021). A new decorrelation phase covariance model for noise reduction in unwrapped interferometric phase stacks. *IEEE Transactions on Geoscience and Remote Sensing*, *59*(12), 10126-10135. doi: 10.1109/TGRS.2021.3050087

Zheng, Y., & Zebker, H. A. (2017). Phase correction of single-look complex radar images for user-friendly efficient interferogram formation. *IEEE Journal of Selected Topics in Applied Earth Observations and Remote Sensing*, *10*, 2694-2701.

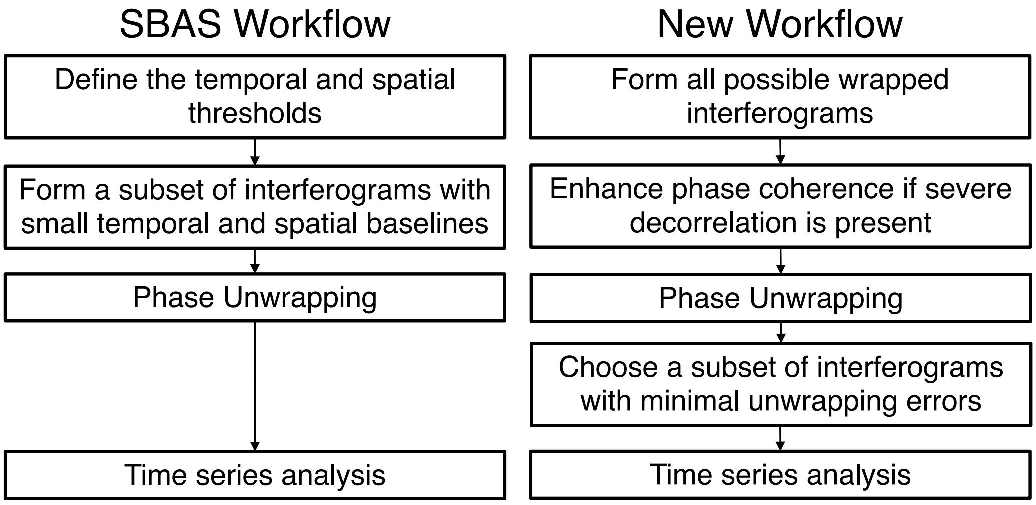

Figure 1. (Left) SBAS InSAR time series analysis workflow. (Right) The new workflow that first mitigates decorrelation noise through InSAR phase reconstruction, then selects the an interferogram subset based on the quality of InSAR phase measurements for time series analysis.

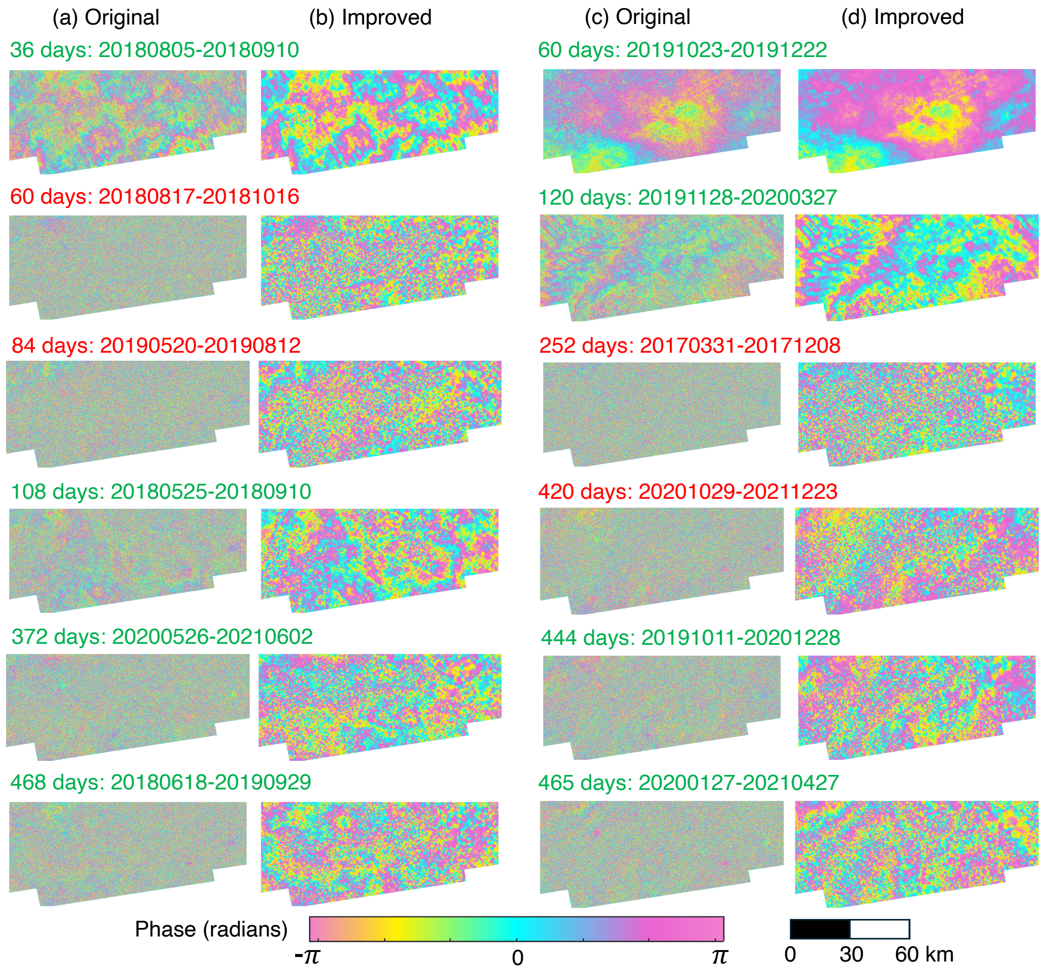

Figure 2. Examples of original interferograms (columns a and c) and reconstructed interferograms (columns b and d) over the Eagle Ford region with varying temporal baselines. Columns a and b use summer Sentinel-1 acquisitions, while columns c and d use Sentinel-1 winter acquisitions. The reconstructed interferograms marked in green were included in the final subset for time series analysis, and the interferograms marked in red were discarded due to relatively large phase unwrapping errors.

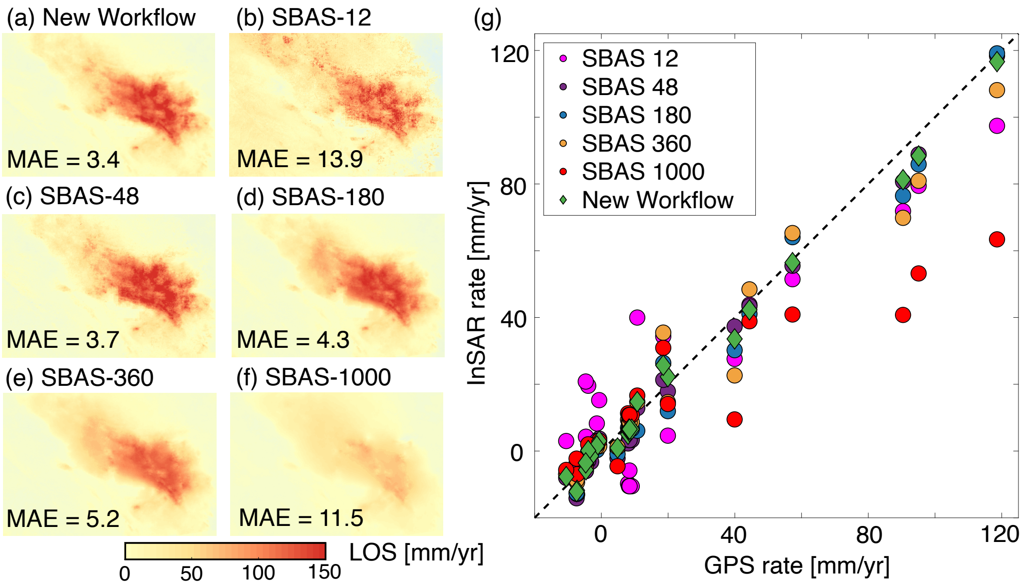

Figure 3. Cumulative line-of-sight (LOS) deformation over the Tulare Basin from 2017-2021 as derived from: (a) a subset of phase reconstructed interferograms with small phase unwrapping errors; and (b-f) a subset of original interferograms with temporal baseline thresholds of 12, 48, 180, 360, and 1000 days. The mean absolute error (MAE) difference of the linear rate estimate (mm/yr) between 24 InSAR and GPS stations over the time period is marked on each deformation solution. Subsidence causes positive LOS deformation (red). (g) Scatter plots of co-located GPS and InSAR LOS deformation rate estimates (mm/yr) derived from different interferogram subsets.

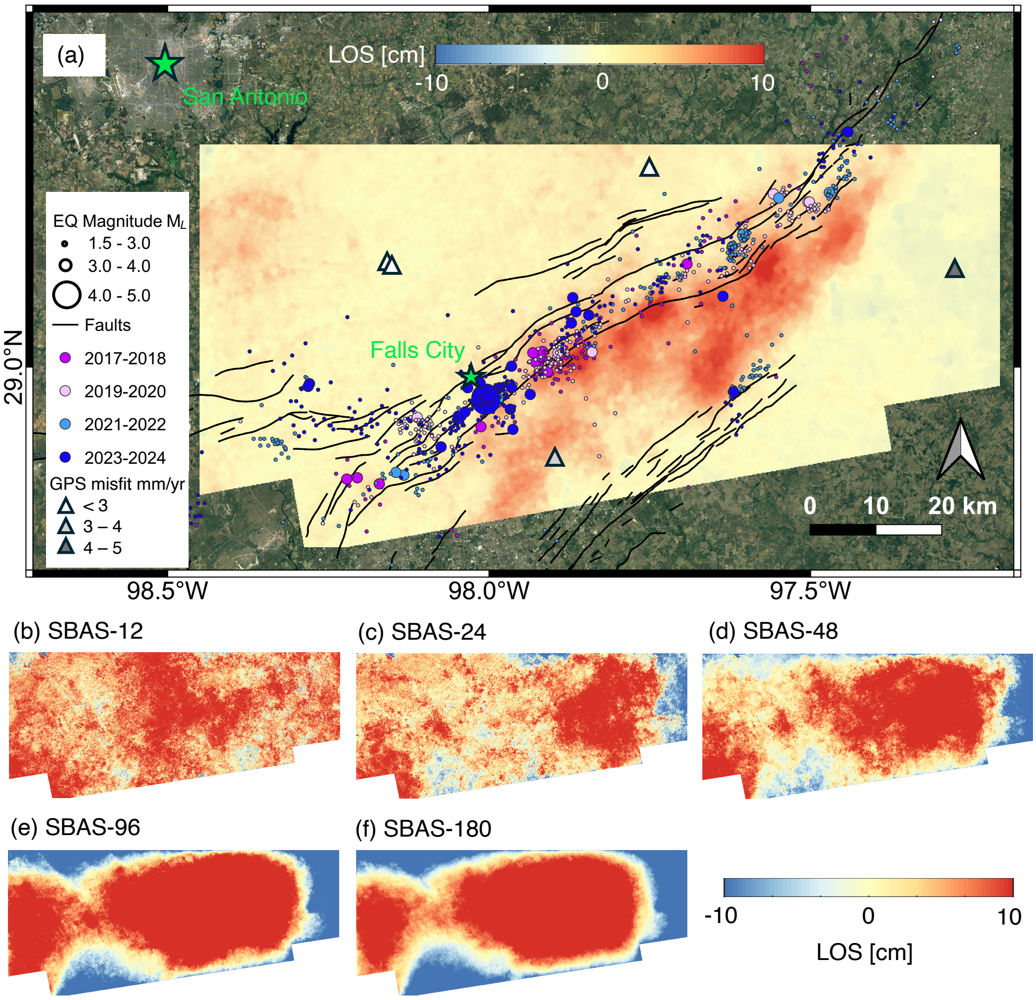

Figure 4. Cumulative line-of-sight (LOS) deformation over the Eagle Frod region between February 2017-December 2021 as derived from: (a) a subset of phase reconstructed interferograms with small phase unwrapping errors. Subsidence leads to positive LOS deformation. The locations and magnitudes of earthquakes since 2017 (circles), mapped faults are from McKeighan et al. (2022), and GPS stations (triangles). A cluster of recent earthquakes (M_L>4.0) occurred near Falls City; and (b-f) original decorrelated interferograms with temporal baseline thresholds of 12, 24, 48, 96, and 180 days.

A robust method for selecting a high-quality interferogram subset in InSAR surface deformation analysis

M. S. Zebker [1*], J. Chen[1,2]

[1]Jackson School of Geosciences, Department of Earth and Planetary Science, The University of Texas at Austin, Austin, TX
[2]Department of Aerospace Engineering and Engineering Mechanics, The University of Texas at Austin, Austin, TX

Key Points:

- InSAR phase coherence does not always decrease with temporal baselines.
- Choosing interferograms based on phase quality rather than temporal baselines better mitigates decorrelation and tropospheric noise.
- The improved InSAR analysis strategy reveals up to 11 cm of deformation signals associated with oil and gas operations over the Eagle Ford.

*Austin, TX

Corresponding author: Molly S. Zebker, mzebker@utexas.edu

Abstract

The accuracy of surface deformation derived from Interferometric Synthetic Aperture Radar (InSAR) observations depends on the quality of the chosen interferogram subset. We present a method to select interferogram subsets based on unwrapping errors rather than temporal baseline thresholds. Using Sentinel-1 interferograms over the Tulare Basin (CA), we show that tropospheric noise dominates short temporal baseline subset solutions (with up to 2.9 cm/yr residuals at co-located GPS sites), while decorrelation leads to a systematic underestimation of true deformation rate in long temporal baseline subset solutions (with up to 5.5 cm/yr residuals). Our new workflow better mitigates these two noise sources at the same time. In the Eagle Ford (TX) region, our strategy revealed up to $\sim$11 cm of cumulative line-of-sight (LOS) deformation over a $\sim$900 km^2 region. This deformation feature is associated with ongoing oil and gas activities and is reported for the first time here.

Plain Language Summary

Deformation estimates are often impacted by noise related to weather conditions and surface vegetation changes. It is common to select an interferogram subset based on a temporal baseline threshold. However, InSAR phase quality may be influenced by other factors such as the weather conditions and surface vegetation rather than temporal baselines. We designed an InSAR processing strategy and applied it to two vegetated regions that experience land subsidence due to agriculture groundwater pumping or oil and gas production. In the Tulare Basin, we showed that deformation estimates are impacted by weather and vegetation related noise and can vary substantially depending on which interferograms are chosen. With our strategy, we better mitigate both noise sources at the same time. In the Eagle Ford region, our workflow revealed up to $\sim$11 cm of surface deformation over a $\sim$900 km^2 area for the first time. This is an oil and gas producing region where production activities have led to an increase in seismicity. Based on these findings, accurate surface deformation derived from InSAR data is now achievable in densely vegetated regions and can play an important role in future induced seismicity studies.

1 Introduction

Interferometric Synthetic Aperture Radar (InSAR) is an imaging radar technique for measuring surface deformation associated with geophysical processes including, but not limited to, tectonics (e.g., Fialko et al., 2002; Wright et al., 2004; Shirzaei & Bürgmann, 2013; Fielding et al., 2017; Xu et al., 2021), volcanism (e.g., Jónsson et al., 2000; Pritchard & Simons, 2002; Hooper et al., 2004; Lundgren et al., 2013), and groundwater hydrology (e.g., Amelung et al., 1999; Hoffmann et al., 2001; Schmidt & Burgmann, 2003; Bell et al., 2008; Chaussard et al., 2014). Achieving millimeter-to-centimeter level accuracy required by many of these studies, however, is challenging due to effects such as decorrelation and atmospheric artifacts. Physical changes in the surface properties between two radar image acquisitions (e.g., vegetation growth and surface disturbance) lead to phase decorrelation (H. A. Zebker & Villasenor, 1992). Phase measurements at completely decorrelated radar pixels do not contain spatially coherent phase information. Conversely, changes in temperature, pressure, and humidity (Bevis et al., 1992) often appear as spatially coherent tropospheric noise, similar to surface deformation signals. While weather models and topography data can be used to estimate and remove the stratified tropospheric noise component (e.g., Doin et al., 2009; Wadge et al., 2002; Jolivet et al., 2011; Li et al., 2009; Bekaert et al., 2015a, 2015b), these approaches often fail to capture the turbulent noise component that is approximately random at time scales greater than a day (Emardson et al., 2003). In many InSAR studies, decorrelation and tropospheric turbulence noise are the two major factors that limit InSAR measurement accuracy.

To mitigate tropospheric and decorrelation noise, Berardino et al. (2002) developed the Small BAseline Subset (SBAS) method to derive surface deformation solutions from a stack of interferograms. The algorithm assumes that interferograms with large temporal baselines (the time between two radar acquisitions used to form the interferogram) often suffer from more severe decorrelation artifacts. Therefore, the use of a temporal baseline threshold in the subset selection can reduce the number of decorrelated phase measurements used in surface deformation analysis. A problem arises in areas with dense vegetation where phase decorrelation occurs even in short baseline interferograms (e.g., 48 or 60 days), which limits the interferogram subset size and ability to reduce other noise terms. To better mitigate decorrelation noise, Persistent Scatterer (PS) algorithms were developed to select pixels that suffer from minimal decorrelation artifacts (e.g., roads, buildings, or bare rock) (e.g., Ferretti et al., 2000; Hooper et al., 2004; Agram, 2010; Huang & Zebker, 2022; Wang & Chen, 2022). In areas with severe decorrelation, only phase measurements at PS pixels are suitable for surface deformation analysis. To further advance the capability of PS interferometry, Ferretti et al. (2011) jointly analyzed nearby pixels (Distributed Scatterers) with homogeneous amplitude distributions (referred to as statistically homogeneous pixels or SHP). The InSAR phase observations from each SHP group are averaged to improve the signal-to-noise-ratio (SNR) and a covariance matrix model (Guarnieri & Tebaldini, 2008) is employed to filter phase measurements for surface deformation analysis.

While different selection criteria are adopted in existing PS/DS algorithms, they often require InSAR phase measurements to remain stable at the identified PS/DS over the entire InSAR observation period. However, even at relatively stable PS/DS pixels, phase measurements are often decorrelated in a portion of the interferograms. It is common to assume interferograms with longer temporal baselines tend to decorrelate more than interferograms with shorter temporal baselines. However, other factors (e.g., weather and surface conditions) may cause decorrelation as well. Based on these observations, we design a processing strategy that selects an interferogram subset for surface deformation analysis based on decorrelation and the associated phase unwrapping errors, regardless of interferogram temporal baselines. This new workflow allows us to enhance phase coherence and reduce decorrelation noise through an optional step that integrates recent phase reconstruction algorithms (e.g., Guarnieri & Tebaldini, 2008; Fornaro et al., 2015; Ansari et al., 2018). This InSAR processing strategy is computationally efficient and easy to implement, and can be incorporated into existing workflows to extend the use of the Small BAseline Subset approaches over densely vegetated areas.

2 Methodology

Interferometric Synthetic Aperture Radar (InSAR) techniques compute the phase difference between two SAR images over the same area of interest. After removing the phase component related to surface topography, the observed InSAR phase at a pixel of interest, $\Delta\phi$, can be written as (Hanssen, 2001):

$$\Delta\phi = \frac{4\pi}{\lambda}\Delta d_{LOS} + \Delta\phi_{orb} + \Delta\phi_{decor} + \Delta\phi_{unwrap} + \Delta\phi_{dem} + \Delta\phi_{iono} + \Delta\phi_{tropo} + \Delta\phi_n \quad (1)$$

where λ is the radar wavelength and Δd_{LOS} is the surface deformation between two SAR acquisition dates along the radar line-of-sight (LOS) direction. The remaining phase terms on the right are InSAR measurement noise due to orbital errors, phase decorrelation and associated unwrapping errors, digital elevation model (DEM) errors, ionospheric and tropospheric artifacts, and other smaller residual noise terms such as thermal or soil moisture effects. Among these noise terms, orbital errors, DEM errors, and ionospheric delays can be corrected during the interferogram formation (e.g., Fattahi & Amelung, 2013; Fattahi et al., 2017). Additionally, stratified tropospheric noise can be estimated and removed using a combination of global or local atmospheric weather models along with zenith tropospheric delay measurements at GNSS sites (e.g., the GACOS correction as described in Yu et al. (2017)). Therefore, our algorithm design focuses on the reduction of decorrelation and the associated phase unwrapping errors (H. A. Zebker & Villasenor, 1992) as well as tropospheric turbulence noise errors (e.g., H. A. Zebker et al., 1997; Emardson et al., 2003).

Given N high-quality interferograms derived from M SAR acquisitions, Berardino et al. (2002) proposed a method to solve for the surface deformation time series at a pixel of interest as:

$$Bv = \Delta\Phi \tag{2}$$

where $v = [v_1, ..., v_{M-1}]^T$ is the vector of unknown mean velocities between each consecutive SAR acquisition, and $\Delta\Phi = [\Delta\phi_1, ..., \Delta\phi_N]^T$ is a $N\times1$ vector of observed InSAR phases at the given pixel. B is the $N\times(M-1)$ system matrix as defined in (Berardino et al., 2002), and we can solve for v as an inverse problem of Equation (2).

Berardino et al. (2002) named this InSAR time series analysis algorithm the Small BAseline Subset (SBAS) method because a subset of N high-quality InSAR observations is chosen for the time series inversion based on user-defined temporal and spatial baseline thresholds (Fig. 1, left). The algorithm was designed based on the fact that interferograms with large temporal or spatial baselines are more likely to suffer from more severe decorrelation noise. Thus, selecting a subset of interferograms with small baselines allows users to limit the total number of decorrelated phase measurements in the InSAR phase vector Φ in Equation (2). By contrast, tropospheric turbulence noise is not correlated with temporal or spatial baselines (e.g., Tymofyeyeva & Fialko, 2015; M. S. Zebker et al., 2023). Because tropospheric turbulence noise can be considered spatially coherent (similar to deformation signals) but random in time between SAR acquisitions (Emardson et al., 2003), it is desirable to include a large number of interferograms acquired on different dates (especially those with long temporal baselines and thus larger secular deformation signals) as input data for the SBAS inversion (Supporting Information S1).

One limitation of the SBAS approach is that the InSAR decorrelation noise level cannot be measured using temporal and spatial baseline alone. In areas with dense vegetation, a short temporal baseline threshold (e.g., 48 or 60 days) is often imposed to limit temporal decorrelation noise due to vegetation growth in the interferogram subset. However, this leads to a substantial reduction in the total number of phase observations used in time series inversion, which limits our ability to mitigate tropospheric noise (e.g., H. A. Zebker et al., 1997; Zheng et al., 2021) and closure phase biases (e.g., Ansari et al., 2021; Zheng et al., 2022). A small portion of interferograms with longer temporal baselines (e.g., a year) often maintain good phase coherence at certain stable pixels such as roads, man-made structures, and barren terrain. These phase observations can improve the accuracy of the SBAS surface deformation estimates. Based on these facts, our new workflow is designed to choose the interferogram subset based on the phase quality of the interferogram, rather than temporal and spatial baseline thresholds (Fig. 1, right). To do this, we first form all possible interferogram pairs. If severe decorrelation noise is present, we enhance InSAR phase quality through phase reconstruction methods such as coherence-based filtering (e.g., Guarnieri & Tebaldini, 2008; Ferretti et al., 2011; Fornaro et al., 2015; Mirzaee et al., 2023) or an interpolation between phase observations at stable PS pixels (e.g., Ferretti et al., 2000; Hooper et al., 2004; Agram, 2010). This increases the total number of interferograms suitable for the time series analysis. The reconstructed interferograms are then unwrapped. Finally, we compute the amount of unwrapping errors for each interferogram and choose a subset of interferograms with small total phase unwrapping errors as input for the time series inversion. For each unwrapped interferogram, we define the phase unwrapping error at a pixel m as:

$$\phi_m^{err} = \sum_k^4 \Delta\phi_{mn}, \text{ if } \Delta\phi_{mn} > \pi \tag{3}$$

where $\Delta\phi_{mn}$ is the unwrapped phase difference between pixel m and n in an interferogram, and pixel n is one of four adjacent pixels to center pixel m. If $\Delta\phi_{mn} < \pi$, the unwrapping error contribution is 0, as defined in C. Chen and Zebker (2001). We compute the total phase unwrapping error of an interferogram as the sum of the phase unwrapping error over all radar pixels (Wang & Chen, 2022).

3 Test Sites and Data Processing

Our first study site is the Tulare Basin in the southern portion of the Central Valley, California (Fig. S1, left), a large agricultural region that has relied on groundwater since the early 1920s (Poland, 1975). The groundwater demand in combination with extended droughts throughout California has led to aquifer sediment compaction and subsequent land subsidence (e.g., Galloway et al., 1999; Faunt et al., 2016). As a result, InSAR techniques have been used to monitor pumping-induced land subsidence and estimate permanent groundwater loss in the region (e.g., Farr & Liu, 2015; Smith et al., 2017; Ojha et al., 2018; Neely et al., 2021). Our second study site is in Central Texas and contains a portion of the Eagle Ford Shale, southeast of the San Antonio-Austin metroplex (Fig. S1, right). The Eagle Ford Shale is a large oil-producing region. The recent ramp-up in shale fracking activities led to increased reliance on groundwater resources from the Carrizo-Wilcox aquifer that overlays the Eagle Ford Shale (Scanlon et al., 2020). This combination of groundwater withdrawal and oil and gas production can produce complex deformation signals. The growth of vegetation at both of these sites can lead to severe decorrelation in interferograms with relatively short temporal baselines (e.g., $\sim$ 2 months), a challenging scenario for InSAR time series analysis. Furthermore, because both sites are located in the mid-latitude and are relatively flat regions, DEM and ionospheric noise terms are not substantial. Given that the primary noise terms are tropospheric turbulence noise and decorrelation, we chose these two sites to demonstrate the advantages of our time series analysis workflow.

For the California case, we processed 122 C-Band Sentinel-1 SAR images (path 137, frame 114) acquired between 2017 and 2021 using a geocoded single-look-complex (SLC) algorithm (e.g., H. A. Zebker, 2017; Zheng & Zebker, 2017). Because Sentinel-1 satellites have precise orbit controls, the spatial baselines of all interferogram pairs are much smaller than the InSAR critical baseline (Rosen et al., 2000). As a result, we did not observe any noticeable spatial decorrelation artifacts, and our analysis is mainly focused on the mitigation of temporal decorrelation noise. Following the new workflow, we generated all 6498 interferogram pairs without any spatial or temporal thresholds. To enhance the spatial coherence of InSAR phase measurements, we selected PS pixels based on the cosine similarity method (Wang & Chen, 2022), performed a phase interpolation among PS pixels (J. Chen et al., 2015), and unwrapped InSAR phase measurements using the Statistical-Cost, Network-flow Algorithm for Phase Unwrapping (SNAPHU) (C. Chen & Zebker, 2001) algorithm. We solved for the long-term deformation trend over the study period based on a linear deformation (constant velocity) model from interferograms with the phase unwrapping error $<$ 10,000 radians. In a control SBAS experiment, we formed interferogram subsets with various temporal baseline thresholds (e.g., 12, 48, 360, and 1000 days). For example, a 48-day interferogram subset contains all interferograms with $<=$ 48-day temporal baselines. For each small baseline subset, we unwrapped InSAR phase measurements using SNAPHU and solved for the cumulative LOS deformation over the study period based on the same linear deformation (constant velocity) model.

For the Texas case, we followed a similar processing strategy and processed 123 C-band Sentinel-1 images (path 107, frame 92). Using the new workflow, we generated all

7503 interferogram pairs without any spatial or temporal thresholds and improved InSAR phase quality through a PS-interpolation. We solved for the cumulative LOS deformation over the study period based on a linear deformation model using a subset of interferograms with the total phase unwrapping error $< 100{,}000$ radians. In a control SBAS experiment, we chose temporal baseline thresholds of 12, 24, 48, 96, and 180 days to form small baseline interferogram subsets. For each small baseline subset, we unwrapped InSAR phase measurements and solved for the cumulative LOS deformation over the study period based on the same linear deformation model.

There are 25 permanent GPS stations with continuous records between 2017 and 2021 over the Tulare Basin (Fig. S1, left). Because InSAR techniques only measure relative deformation with respect to a reference pixel, we chose the GPS station P544 as the reference point to calibrate and used the remaining 24 GPS stations as controls to validate InSAR results. We projected the GPS daily East, North, and Up (ENU) time series (independently processed by the Nevada Geodetic Laboratory) to the radar LOS direction and estimated the average surface deformation rate in mm/year from both GPS and InSAR observations. We used the InSAR and GPS rate misfit, Δ_v to quantify the uncertainty in InSAR surface deformation solutions derived from different subsets. Similarly, we chose the GPS station TXFL as the reference point for the Texas case and used the remaining 5 stations as independent controls to validate InSAR results (Fig. S1, right).

4 Results and Discussion

4.1 The relationship between phase quality and temporal baselines

The Tulare Basin and Eagle Ford sites are covered with dense vegetation and the vegetation growth between radar acquisitions causes severe decorrelation, which appears random in space (e.g., Fig. 2 columns a and c). The InSAR phase measurement at a severely decorrelated radar pixel can be considered a random wrapped phase value between 0 and 2π, and no longer contains spatially coherent phase information such as surface deformation signals or tropospheric noise. Unwrapping interferograms with severe decorrelation artifacts is time-consuming and unreliable, and often introduces large phase unwrapping errors that dominate in the final InSAR time series solutions. We emphasize that not all radar pixels decorrelate at the same rate. For example, roads, buildings, and rock outcrops can remain coherent over a much longer period of time than agricultural field pixels. Therefore, we identified phase measurements at relatively stable PS pixels and interpolated between PS pixels to improve InSAR spatial phase coherence (e.g., Fig. 2 columns b and d) and reduced unwrapping time (Table S1).

An important finding of this study is that temporal baseline is not always a robust measure for selecting the interferogram subset (Fig. 2). For the Texas case, some reconstructed interferograms with longer temporal baselines (e.g., over 400 days) contain smaller phase unwrapping errors than those with shorter temporal baselines (e.g., 60 days). We found that interferograms formed from winter SAR scenes often have better phase coherence than interferograms formed from summer SAR scenes. This is because after deciduous trees lose their leaves in the fall, radar signals reflected from tree trunks can maintain coherence over a long period of time. Furthermore, some radar images contain large tropospheric noise anomalies due to heat waves or tropical storms (Staniewicz et al., 2020). Interferograms formed using these radar images tend to suffer from severe decorrelation noise regardless of temporal baselines. In summary, we identified a total of 2360 (out of 7503) interferograms with phase unwrapping errors $< 100{,}000$ radians for the Texas case. Among these interferograms, there are 865 that span >200 days and 188 interferograms that span >1 year. For the California case, we identified a total of 527 (out of 6389) interferograms with phase unwrapping errors $< 10{,}000$ radians. Among those interferograms, 127 interferograms span >60 days and 7 span >90 days. We imposed a smaller total phase unwrapping error threshold for the California case because: (1) while dense vegetation is only present over a portion of the Tulare Basin site covered with agricultural fields, it is present over the entire Eagle Ford site (Fig. S1). Therefore, the total phase unwrapping error is smaller in the Tulare Basin interferograms than in the Eagle Ford interferograms when similar decorrelation artifacts occur; and (2) the expected subsidence trend is much larger at the Tulare Basin site than the Eagle Ford site. Fewer interferograms are required to reduce tropospheric noise in order to reconstruct a larger deformation signal. In addition, interferograms with large deformation signals (e.g. Tulare Basin interferograms with long temporal baselines) may be prone to aliasing because the density of high-quality InSAR pixels is too low to capture the rapidly changing InSAR fringes (Pepin & Zebker, 2024).

4.2 The Tulare Basin results

The Tulare Basin LOS deformation estimates derived from a subset of interferograms with small phase unwrapping errors show up to 150 mm/yr LOS deformation (Fig. 3a) with a mean absolute error (MAE) of 3.4 mm/yr and a maximum absolute error of 9.1 mm/yr based on independent GPS validation (Fig. 3g and Table S2). The observed deformation pattern is geographically consistent with recent InSAR studies (e.g., Farr, 2018; Murray & Lohman, 2018; Ojha et al., 2019; Neely et al., 2021; Kang & Knight, 2023). For example, Neely et al. (2021) analyzed 263 Sentinel-1 interferograms (with temporal baselines < 100 days) and observed up to ~ 270 mm/yr subsidence between April 2015 and October 2017. The average velocity residual was 2.9 mm/yr based on independent GPS validation. They found that the subsidence rate changes throughout the year in response to water demand. Up to 345 mm/yr vertical subsidence (with an average velocity residual of 6.4 mm/yr) was observed during the dry period of October 2015 - September 2016, while up to 177 mm/yr vertical subsidence (with an average velocity residual of 11.1 mm/yr) was observed during the wet period of October 2016 - September 2017. Ojha et al. (2019) and Kang and Knight (2023) reported similar error residuals but different rate magnitudes, likely due to differences in the study period and InSAR processing methodologies.

To further illustrate how the InSAR processing strategy may influence SBAS solutions, Fig. 3b-f shows the LOS surface deformation rate estimates derived from different small baseline subsets. The deformation solution derived from the 12-day interferogram subset (denoted as "SBAS-12') shows an MAE of 13.9 mm/yr and a maximum absolute error of 29.2 mm/yr (Fig. 3g and Table S2). Given that we observed minimal decorrelation artifacts (thus minimal phase unwrapping errors) in 12-day interferograms, the errors in the SBAS-12 solution are primarily due to tropospheric noise. The SBAS-48 solution shows an MAE of 3.7 mm/yr and a maximum absolute error of 9.7 mm/yr, which is comparable to the deformation solution derived from the interferogram subset with small phase unwrapping errors. We again observed minimal decorrelation artifacts in the SBAS-48 interferogram subset, and tropospheric noise is the primary error source. In this case, interferograms with longer temporal baselines contain larger secular deformation signals than interferograms with shorter temporal baselines, while the tropospheric noise level among these interferograms is similar. As a result, the inclusion of interferograms with longer temporal baselines can better reduce the residual tropospheric noise level in the SBAS deformation rate estimates (Supporting Information S1). However, the deformation solutions derived from a subset of interferograms with temporal baselines up to 180, 360, and 1000 days have an increasing MAE of 4.3, 5.2, and 11.5 mm/yr. This is because decorrelation artifacts are observed in interferograms with temporal baselines ~ 2 months and longer. As the temporal baseline threshold increases, more decorrelated InSAR phase observations are used in the SBAS inversion. In particular, most of the interferograms in the SBAS-1000 subset are completely decorrelated over the agricultural fields. As a result, fitting a linear deformation model to decorrelated InSAR observations may yield a near-zero deformation rate estimate when the number of decorrelated observations is sufficiently large. A systematic underestimation (up to 55.2 mm/yr) was observed in the SBAS-1000 solution at all GPS stations where a non-trivial deformation signal is present (Fig. 3g and Table S2). We emphasize it is important to evaluate the accuracy of InSAR deformation estimates at GPS stations where non-trivial deformation is present. Because a large number of random decorrelated InSAR observations may yield near-zero deformation rate estimates, they often appear to be "consistent" with GPS observations at relatively stable locations. However, this does not mean decorrelated InSAR measurements contain any information about the true deformation signals, and they should be excluded in the SBAS inversion.

4.3 The Eagle Ford region results

The Eagle Ford LOS deformation estimates derived from a subset of interferograms with small phase unwrapping error reveals a $\sim$900 km^2 region of up to 11 cm of cumulative LOS deformation between February 2017 and December 2021 (Fig. 4a). The MAE at 5 GPS permanent stations is 2.7 mm/year and a maximum absolute error is 4.8 mm/year at TXCU (Fig. 4a and Table S3). The observed subsidence signal (Fig. 4a) aligns well with oil and gas production wells (The Railroad Commission of Texas, 2023). This region experienced a ramp-up in oil and gas production around 2010. Approximately 20-25 million barrels of oil (bbl) and 100-120 million one thousand cubic feet (mcf) of gas were produced every month since 2014 (The Railroad Commission of Texas, 2023). Similarly, comparable volumes of subsurface water are co-produced with oil and gas. Approximately 1246 million bbl of water from unconventional wells was produced from 2009-2016 in the Eagle Ford with 337, 291, and 206 million bbl of produced water each year for 2014, 2015, and 2016 respectively (Scanlon et al., 2019). Here, it is likely that the production of water, oil, and gas all contribute to the observed land subsidence (Fig. S2).

In contrast, the LOS surface deformation rate estimates derived from different small baseline subsets failed to detect this large deformation signal (Fig. 4b-f). The SBAS solution derived from the 12-day interferogram subset (Fig. 4b) has an MAE of 5.5 mm/yr and a maximum absolute error of 16 mm/yr. Given that we observed minimal decorrelation artifacts in the 12-day interferograms (e.g., Fig. S3a and g), the residuals are mostly due to tropospheric noise. We note that there are only five GPS validation stations over the Eagle Ford region. As a result, the GPS-InSAR misfit only represents the InSAR measurement accuracy at these five locations (Table S3), and InSAR noise residuals can be much larger over regions with visible tropospheric noise artifacts. Because the study site is densely vegetated, we observed decorrelation artifacts and associated phase unwrapping errors even in some 24-day interferograms (Fig. S3h). As a result, both tropospheric noise and decorrelation artifacts are present in the SBAS-24 solution, and decorrelation-related artifacts dominate in the SBAS-48, SBAS-96, and SBAS-180 solutions. While unwrapping errors often lead to a systematic underestimation of the true deformation rate (e.g., in the Tulare Basin case Fig. 3f), decorrelation signatures can sometimes be unpredictable. In the Eagle Ford case, very large phase unwrapping errors are present in a subset of interferograms, which produced unrealistic artifacts in the SBAS-48, SBAS-96, and SBAS-180 solutions. We emphasize that it is important to employ a phase reconstruction technique to enhance phase quality prior to the surface deformation analysis over densely vegetated areas such as the Eagle Ford region. However, some long temporal baseline interferograms are reconstructed successfully, while some short temporal baseline interferograms fail to be reconstructed (Fig. 2). Therefore, selecting interferograms based on an unwrapping error threshold is more robust than a temporal baseline threshold over regions with large tropospheric noise and severe decorrelation artifacts.

While there are numerous InSAR surface deformation studies over the less vegetated Permian Basin in West Texas (Kim & Lu, 2018; Staniewicz et al., 2020; Zhai et al., 2021; Hennings et al., 2021; Pepin et al., 2022), our study is the first that observes a large subsidence feature with spatially dense information over the Eagle Ford region in Central Texas. Surface deformation can be used to derive subsurface stress and pore pressure changes related to oil and gas injection and extraction (e.g., Yang et al., 2015; Vasco et al., 2016; Shirzaei et al., 2019; Deng et al., 2020). These changes in the subsurface can eventually result in fault slip and trigger earthquakes (Segall, 1989). For example, Frohlich and Brunt (2013) reported 62 earthquakes in the Eagle Ford region from 2009-2011, highlighted by a M_w 4.8 earthquake in October 2011 in Fashing, TX. They found that most of the seismicity followed fluid extraction, not injection. Recently, the Eagle Ford region has experienced a noticeable increase in seismic activity, and there were 165, 341, 336, 349 earthquakes recorded in 2017-2018, 2019-2020, 2021-2022, 2023-March 13, 2024, respectively (Fig. 4a) (TexNet, 2024). In particular, two earthquakes (M_L 4.3 and M_L 4.7) occurred on February 17, 2024 near Falls City, which were felt by many San Antonio and Austin residents. The increase in magnitude and frequency of these large seismic events requires further scientific investigation, and InSAR data can play an important role in these future induced seismicity studies.

5 Conclusion

In this study, we found that selecting an interferogram subset based on phase quality rather than temporal baseline leads to better mitigation of decorrelation and tropospheric noise. In the Tulare Basin case, our InSAR processing strategy generated a deformation solution comparable to the SBAS solution when the optimal temporal baseline threshold was employed. In the Eagle Ford case, our processing strategy revealed a large subsidence signature associated with oil and gas operations that is otherwise undetectable due to the presence of large tropospheric noise and severe decorrelation artifacts. Our workflow is easy to implement, which can extend the use of the SBAS algorithm over humid and densely vegetated terrain that is challenging for InSAR studies.

6 Open Research

Sentinel-1 SAR imagery over the Tulare Basin, CA (path 137, frame 114) and Eagle Ford region, TX (path 107, frame 92) can be queried and downloaded from the Alaska Satellite Facility at https://search.asf.alaska.edu. Interferograms with comparable quality can be produced using InSAR processing packages such as the InSAR Scientific Computing Environment 3 (ISCE3) (Rosen et al., 2018), GMTSAR (Sandwell et al., 2011), or GAMMA (Wegmüller et al., 2016). GPS data were processed by the Nevada Geodetic Laboratory and downloaded at http://geodesy.unr.edu/NGLStationPages/GlobalStationList (Blewitt et al., 2018). A list of available GPS stations over the Tulare Basin and the Eagle Ford region can be found in the Supporting Information.

Acknowledgments

This research was funded by the NASA Earth Surface and Interior Program grant numbers 80NSSC18K0467 and 80NSSC22K0412.

References

Agram, P. (2010, 01). Persistent scatterer interferometry in natural terrain.

Amelung, F., Galloway, D. L., Bell, J. W., Zebker, H. A., & Laczniak, R. J. (1999, 06). Sensing the ups and downs of Las Vegas: InSAR reveals structural control of land subsidence and aquifer-system deformation. *Geology*, *27*(6), 483-486. Retrieved from `https://doi.org/10.1130/0091-7613(1999)027<0483:STUADO>2.3.CO;2` doi: 10.1130/0091-7613(1999)027⟨0483:STUADO⟩2.3.CO;2

Ansari, H., De Zan, F., & Bamler, R. (2018). Efficient phase estimation for interferogram stacks. *IEEE Transactions on Geoscience and Remote Sensing*, *56*(7), 4109-4125. doi: 10.1109/TGRS.2018.2826045

Ansari, H., De Zan, F., & Parizzi, A. (2021). Study of systematic bias in measuring surface deformation with SAR interferometry. *IEEE Transactions on Geoscience and Remote Sensing*, *59*(2), 1285-1301. doi: 10.1109/TGRS.2020.3003421

Bekaert, D., Hooper, A., & Wright, T. J. (2015a). A spatially variable power law tropospheric correction technique for InSAR data. *Journal of Geophysical Research: Solid Earth*, *120*(2), 1345-1356. Retrieved from `https://agupubs.onlinelibrary.wiley.com/doi/abs/10.1002/2014JB011558` doi: https://doi.org/10.1002/2014JB011558

Bekaert, D., Walters, R., Wright, T., Hooper, A., & Parker, D. (2015b, 09). Statistical comparison of InSAR tropospheric correction techniques. *Remote Sensing of Environment*, *170*, 40–47. doi: 10.1016/j.rse.2015.08.035

Bell, J., Amelung, F., Ferretti, A., Bianchi, M., & Novali, F. (2008, 02). Permanent scatterer InSAR reveals seasonal and long-term aquifer-system response to groundwater pumping and artificial recharge. *Water Resources Research*, *44*. doi: 10.1029/2007WR006152

Berardino, P., Fornaro, G., Lanari, R., & Sansosti, E. (2002). A new algorithm for surface deformation monitoring based on small baseline differential SAR interferograms. *IEEE Transactions on Geoscience and Remote Sensing*, *40*(11), 2375-2383. doi: 10.1109/TGRS.2002.803792

Bevis, M., Businger, S., Herring, T. A., Rocken, C., Anthes, R. A., & Ware, R. H. (1992). GPS meteorology: Remote sensing of atmospheric water vapor using the global positioning system. *Journal of Geophysical Research: Atmospheres*, *97*(D14), 15787-15801. Retrieved from `https://agupubs.onlinelibrary.wiley.com/doi/abs/10.1029/92JD01517` doi: https://doi.org/10.1029/92JD01517

Blewitt, G., Hammond, W. C., & Kreemer, C. (2018). Harnessing the GPS data explosion for interdisciplinary science. *EOS*, *99*. doi: https://doi.org/10.1029/2018EO104623

Chaussard, E., Bürgmann, R., Shirzaei, M., Fielding, E. J., & Baker, B. (2014). Predictability of hydraulic head changes and characterization of aquifer-system and fault properties from InSAR-derived ground deformation. *Journal of Geophysical Research: Solid Earth*, *119*(8), 6572-6590. Retrieved from `https://agupubs.onlinelibrary.wiley.com/doi/abs/10.1002/2014JB011266` doi: https://doi.org/10.1002/2014JB011266

Chen, C., & Zebker, H. (2001, 03). Two-dimensional phase unwrapping with use of statistical models for cost functions in nonlinear optimization. *Journal of the Optical Society of America. A, Optics, image science, and vision*, *18*, 338-51. doi: 10.1364/JOSAA.18.000338

Chen, J., Zebker, H. A., & Knight, R. (2015). A persistent scatterer interpolation for retrieving accurate ground deformation over InSAR-decorrelated agricultural fields. *Geophysical Research Letters*, *42*(21), 9294-9301. Retrieved from `https://agupubs.onlinelibrary.wiley.com/doi/abs/10.1002/2015GL065031` doi: https://doi.org/10.1002/2015GL065031

Deng, F., Dixon, T. H., & Xie, S. (2020). Surface deformation and induced seismicity due to fluid injection and oil and gas extraction in Western Texas. *Journal of Geophysical Research: Solid Earth*, *125*(5), e2019JB018962. Retrieved from `https://agupubs.onlinelibrary.wiley.com/doi/abs/10.1029/2019JB018962` (e2019JB018962 2019JB018962) doi: https://doi.org/10.1029/2019JB018962

Doin, M., Lasserre, C., Peltzer, G., Cavalié, O., & Doubre, C. (2009). Corrections of stratified tropospheric delays in SAR interferometry: Validation with global atmospheric models. *Journal of Applied Geophysics*, *69*(1), 35-50.

Retrieved from https://www.sciencedirect.com/science/article/pii/S0926985109000603 (Advances in SAR Interferometry from the 2007 Fringe Workshop) doi: https://doi.org/10.1016/j.jappgeo.2009.03.010

Emardson, T., Simons, M., & Webb, F. (2003, 05). Neural atmospheric delay in interferometric Synthetic Aperture Radar applications: statistical description and mitigation. *Journal of Geophysical Research*, *108*. doi: 10.1029/2002JB001781

Farr, T. G. (2018). InSAR measurements of subsidence and rebound in California. In *IGARSS 2018 - 2018 IEEE International Geoscience and Remote Sensing Symposium* (p. 8401-8403). IEEE.

Farr, T. G., & Liu, Z. (2015). Monitoring subsidence associated with ground water dynamics in the Central Valley of California using interferometric radar. *Geophysical Monograph*, *206*, 397-406.

Fattahi, H., & Amelung, F. (2013). DEM error correction in InSAR time series. *IEEE Transactions on Geoscience and Remote Sensing*, *51*(7), 4249-4259. doi: 10.1109/TGRS.2012.2227761

Fattahi, H., Simons, M., & Agram, P. (2017). InSAR time-series estimation of the ionospheric phase delay: An extension of the split range-spectrum technique. *IEEE Transactions on Geoscience and Remote Sensing*, *55*(10), 5984-5996. doi: 10.1109/TGRS.2017.2718566

Faunt, C. C., Sneed, M., Traum, J., & Brandt, J. T. (2016). Water availability and land subsidence in the Central Valley, California, USA. *Hydrogeology journal*, *24*(3), 675-684.

Ferretti, A., Fumagalli, A., Novali, F., Prati, C., Rocca, F., & Rucci, A. (2011). A new algorithm for processing interferometric data-stacks: SqueeSAR. *IEEE Transactions on Geoscience and Remote Sensing*, *49*(9), 3460-3470. doi: 10.1109/TGRS.2011.2124465

Ferretti, A., Prati, C., & Rocca, F. (2000). Nonlinear subsidence rate estimation using permanent scatterers in differential SAR interferometry. *IEEE Transactions on Geoscience and Remote Sensing*, *38*(5), 2202-2212. doi: 10.1109/36.868878

Fialko, Y., Sandwell, D., Agnew, D., Simons, M., Shearer, P., & Minster, B. (2002). Deformation on nearby faults induced by the 1999 Hector Mine earthquake. *Science*, *297*(5588), 1858-1862. Retrieved from https://www.science.org/doi/abs/10.1126/science.1074671 doi: 10.1126/science.1074671

Fielding, E., Sangha, S., Bekaert, D., Samsonov, S., & Chang, J. (2017, 07). Surface deformation of North-Central Oklahoma related to the 2016 Mw 5.8 Pawnee earthquake from SAR interferometry time series. *Seismological Research Letters*, *88*, 971-982. doi: 10.1785/0220170010

Fornaro, G., Verde, S., Reale, D., & Pauciullo, A. (2015). CAESAR: An approach based on covariance matrix decomposition to improve multibaseline–multitemporal interferometric SAR processing. *IEEE Transactions on Geoscience and Remote Sensing*, *53*(4), 2050-2065. doi: 10.1109/TGRS.2014.2352853

Frohlich, C., & Brunt, M. (2013). Two-year survey of earthquakes and injection/production wells in the Eagle Ford Shale, Texas, prior to the MW4.8 20 October 2011 earthquake. *Earth and Planetary Science Letters*, *379*, 56-63. Retrieved from https://www.sciencedirect.com/science/article/pii/S0012821X13004007 doi: https://doi.org/10.1016/j.epsl.2013.07.025

Galloway, D. L., Jones, D. R. D. R., & Ingebritsen, S. E. (1999). *Land subsidence in the United States / edited by Devin Galloway, David R. Jones, S.E. Ingebritsen.* Reston, VA: U.S. Geological Survey.

Guarnieri, A. M., & Tebaldini, S. (2008). On the exploitation of target statistics for SAR interferometry applications. *IEEE Transactions on Geoscience and Remote Sensing*, *46*(11), 3436-3443. doi: 10.1109/TGRS.2008.2001756

Hanssen, R. (2001). *Radar interferometry: Data interpretation and error analysis.* Springer.

Hennings, P., Dvory, N., Horne, E., Li, P., Savvaidis, A., & Zoback, M. (2021, 08). Stability of the Fault Systems That Host-Induced Earthquakes in the Delaware Basin of West Texas and Southeast New Mexico. *The Seismic Record*, *1*(2), 96-106. Retrieved from https://doi.org/10.1785/0320210020 doi: 10.1785/0320210020

Hoffmann, J., Zebker, H., Galloway, D., & Amelung, F. (2001, 06). Seasonal subsidence and rebound in Las Vegas Valley, Nevada, observed by Synthetic Aperture Radar Interferometry. *Water Resources Research*, *37*, 1551-1566. doi: 10.1029/2000WR900404

Hooper, A., Zebker, H., Segall, P., & Kampes, B. (2004). A new method for measuring deformation on volcanoes and other natural terrains using InSAR persistent scatterers. *Geophysical Research Letters*, *31*(23). Retrieved from https://agupubs.onlinelibrary.wiley.com/doi/abs/10.1029/2004GL021737 doi: https://doi.org/10.1029/2004GL021737

Huang, S. A., & Zebker, H. A. (2022). InSAR time-series analysis with a non-Gaussian detector for persistent scatterers. *IEEE Journal of Selected Topics in Applied Earth Observations and Remote Sensing*, *15*, 9208-9225. doi: 10.1109/JSTARS.2022.3216964

Jolivet, R., Grandin, R., Lasserre, C., Doin, M.-P., & Peltzer, G. (2011). Systematic InSAR tropospheric phase delay corrections from global meteorological reanalysis data. *Geophysical Research Letters*, *38*(17). Retrieved from https://agupubs.onlinelibrary.wiley.com/doi/abs/10.1029/2011GL048757 doi: https://doi.org/10.1029/2011GL048757

Jónsson, S., Amelung, F., Zebker, H., & Segall, P. (2000). Widespread uplift and 'trapdoor' faulting on galápagos volcanoes observed with radar interferometry. *Nature (London)*, *407*(6807), 993-996.

Kang, S., & Knight, R. (2023). Isolating the poroelastic response of the groundwater system in InSAR data from the Central Valley of California. *Geophysical Research Letters*, *50*(9), e2023GL103222. Retrieved from https://agupubs.onlinelibrary.wiley.com/doi/abs/10.1029/2023GL103222 (e2023GL103222 2023GL103222) doi: https://doi.org/10.1029/2023GL103222

Kim, J.-W., & Lu, Z. (2018, 03). Association between localized geohazards in West Texas and human activities, recognized by Sentinel-1A/B satellite radar imagery. *Scientific Reports*, *8*. doi: 10.1038/s41598-018-23143-6

Li, Z., Fielding, E. J., Cross, P., & Preusker, R. (2009). Advanced InSAR atmospheric correction: MERIS/MODIS combination and stacked water vapour models. *International Journal of Remote Sensing*, *30*(13), 3343-3363. Retrieved from https://doi.org/10.1080/01431160802562172 doi: 10.1080/01431160802562172

Lundgren, P., Poland, M., Miklius, A., Orr, T., Yun, S.-H., Fielding, E., ... Owen, S. (2013). Evolution of dike opening during the march 2011 kamoamoa fissure eruption, kīlauea volcano, hawai'i. *Journal of Geophysical Research: Solid Earth*, *118*(3), 897-914. Retrieved from https://agupubs.onlinelibrary.wiley.com/doi/abs/10.1002/jgrb.50108 doi: https://doi.org/10.1002/jgrb.50108

McKeighan, C., Hennings, P., Horne, E. A., Smye, K., & Morris, A. (2022, 10). Understanding Anthropogenic Fault Rupture in the Eagle Ford Region, South-Central Texas. *Bulletin of the Seismological Society of America*, *112*(6), 2870-2889. Retrieved from https://doi.org/10.1785/0120220074 doi: 10.1785/0120220074

Mirzaee, S., Amelung, F., & Fattahi, H. (2023). Non-linear phase linking using joined distributed and persistent scatterers. *Computers Geosciences*, *171*, 105291. Retrieved from https://www.sciencedirect.com/science/article/

pii/S0098300422002400 doi: https://doi.org/10.1016/j.cageo.2022.105291

Murray, K. D., & Lohman, R. B. (2018). Short-lived pause in Central California subsidence after heavy winter precipitation of 2017. *Science Advances*, *4*(8), eaar8144. Retrieved from https://www.science.org/doi/abs/10.1126/sciadv.aar8144 doi: 10.1126/sciadv.aar8144

Neely, W. R., Borsa, A. A., Burney, J. A., Levy, M. C., Silverii, F., & Sneed, M. (2021). Characterization of groundwater recharge and flow in California's San Joaquin Valley from InSAR-observed surface deformation. *Water resources research*, *57*(4), e2020WR028451-n/a.

Ojha, C., Shirzaei, M., Werth, S., Argus, D. F., & Farr, T. G. (2018). Sustained groundwater loss in California's Central Valley exacerbated by intense drought periods. *Water Resources Research*, *54*(7), 4449-4460. Retrieved from https://agupubs.onlinelibrary.wiley.com/doi/abs/10.1029/2017WR022250 doi: https://doi.org/10.1029/2017WR022250

Ojha, C., Werth, S., & Shirzaei, M. (2019). Groundwater loss and aquifer system compaction in San Joaquin Valley during 2012–2015 drought. *Journal of Geophysical Research: Solid Earth*, *124*(3), 3127-3143. Retrieved from https://agupubs.onlinelibrary.wiley.com/doi/abs/10.1029/2018JB016083 doi: https://doi.org/10.1029/2018JB016083

Pepin, K., Ellsworth, W., Sheng, Y., & Zebker, H. (2022, 02). Shallow aseismic slip in the Delaware Basin determined by Sentinel-1 InSAR. *Journal of Geophysical Research: Solid Earth*, *127*. doi: 10.1029/2021JB023157

Pepin, K., & Zebker, H. (2024). Aliasing in InSAR 2d phase unwrapping and time series. *IEEE Transactions on Geoscience and Remote Sensing*, 1-1. doi: 10.1109/TGRS.2024.3359482

Poland, J. F. J. F. (1975). *Land subsidence, in the San Joaquin Valley, California, as of 1972 / by J. F. Poland [and three others]; prepared in cooperation with the California Department of Water Resources.* Washington: United States Department of the Interior, Geological Survey.

Pritchard, M., & Simons, M. (2002, 08). A satellite geodetic survey of large scale deformation of volcanic centers in the Central Andes. *Nature*, *418*, 167-71. doi: 10.1038/nature00872

Rosen, P., Gurrola, E. M., Agram, P., Cohen, J., Lavalle, M., Riel, B. V., ... Buckley, S. M. (2018). The insar scientific computing environment 3.0: A flexible framework for nisar operational and user-led science processing. In *Igarss 2018 - 2018 ieee international geoscience and remote sensing symposium* (p. 4897-4900). doi: 10.1109/IGARSS.2018.8517504

Rosen, P., Hensley, S., Joughin, I., Li, F., Madsen, S., Rodriguez, E., & Goldstein, R. (2000, 04). Synthetic aperture radar interferometry. *Proceedings of the IEEE*, *88*, 333 - 382. doi: 10.1109/5.838084

Sandwell, D., Mellors, R., Tong, X., Wei, M., & Wessel, P. (2011). Gmtsar: An insar processing system based on generic mapping tools.

Scanlon, B., Ikonnikova, S., Qian, Y., & Reedy, R. (2020, 02). Will water issues constrain oil and gas production in the U.S.? *Environmental Science Technology*, *54*, 3510–3519. doi: 10.1021/acs.est.9b06390

Scanlon, B., Weingarten, M., Murray, K., & Reedy, R. (2019). Managing basin-scale fluid budgets to reduce injection-induced seismicity from the recent u.s. shale oil revolution. *Seismological research letters*, *90*(1), 171-182.

Schmidt, D., & Burgmann, R. (2003, 09). Time-dependent land uplift and subsidence in the Santa Clara valley, California, from a large interferometric synthetic aperture radar data set. *Journal of Geophysical Research*, *108*. doi: 10.1029/2002JB002267

Segall, P. (1989). Earthquakes triggered by fluid extraction. *Geology*, *17*(10), 942-946. Retrieved from https://doi.org/10.1130/0091-7613(1989)017<0942:ETBFE>2.3.CO;2 doi: 10.1130/0091-7613(1989)017⟨0942:ETBFE⟩2.3.CO;2

Shirzaei, M., & Bürgmann, R. (2013). Time-dependent model of creep on the Hayward fault from joint inversion of 18 years of InSAR and surface creep data. *Journal of Geophysical Research: Solid Earth*, *118*(4), 1733-1746. Retrieved from https://agupubs.onlinelibrary.wiley.com/doi/abs/10.1002/jgrb.50149 doi: https://doi.org/10.1002/jgrb.50149

Shirzaei, M., Manga, M., & Zhai, G. (2019). Hydraulic properties of injection formations constrained by surface deformation. *Earth and Planetary Science Letters*, *515*, 125-134. Retrieved from https://www.sciencedirect.com/science/article/pii/S0012821X19301736 doi: https://doi.org/10.1016/j.epsl.2019.03.025

Smith, R. G., Knight, R., Chen, J., Reeves, J. A., Zebker, H. A., Farr, T., & Liu, Z. (2017). Estimating the permanent loss of groundwater storage in the southern San Joaquin Valley, California. *Water Resources Research*, *53*(3), 2133-2148. Retrieved from https://agupubs.onlinelibrary.wiley.com/doi/abs/10.1002/2016WR019861 doi: https://doi.org/10.1002/2016WR019861

Staniewicz, S., Chen, J., Lee, H., Olson, J., Savvaidis, A., Reedy, R., ... Hennings, P. (2020). InSAR reveals complex surface deformation patterns over an 80,000km2 oil-producing region in the Permian Basin. *Geophysical Research Letters*, *47*(21), e2020GL090151. Retrieved from https://agupubs.onlinelibrary.wiley.com/doi/abs/10.1029/2020GL090151 (e2020GL090151 10.1029/2020GL090151) doi: https://doi.org/10.1029/2020GL090151

TexNet. (2024). *TexNet High Resolution Earthquake Catalog: Bureau for Economic Geology at University of Texas at Austin.* Retrieved 2024-03-28, from https://doi.org/10.15781/76hj-ed46

The Railroad Commission of Texas. (2023). *Eagle Ford Shale.* Retrieved 2024-03-28, from https://www.rrc.texas.gov/oil-and-gas/major-oil-and-gas-formations/eagle-ford-shale/

Tymofyeyeva, E., & Fialko, Y. (2015). Mitigation of atmospheric phase delays in InSAR data, with application to the eastern California shear zone. *Journal of Geophysical Research: Solid Earth*, *120*(8), 5952-5963. Retrieved from https://agupubs.onlinelibrary.wiley.com/doi/abs/10.1002/2015JB011886 doi: https://doi.org/10.1002/2015JB011886

Vasco, D., Harness, P., Pride, S., & Hoversten, M. (2016, 12). Estimating fluid-induced stress change from observed deformation. *Geophysical Journal International*, *208*(3), 1623-1642. Retrieved from https://doi.org/10.1093/gji/ggw472 doi: 10.1093/gji/ggw472

Wadge, G., Webley, P. W., James, I. N., Bingley, R., Dodson, A., Waugh, S., ... Clarke, P. J. (2002). Atmospheric models, GPS and InSAR measurements of the tropospheric water vapour field over Mount Etna. *Geophysical Research Letters*, *29*(19), 11-1-11-4. Retrieved from https://agupubs.onlinelibrary.wiley.com/doi/abs/10.1029/2002GL015159 doi: https://doi.org/10.1029/2002GL015159

Wang, K., & Chen, J. (2022). Accurate persistent scatterer identification based on phase similarity of radar pixels. *IEEE Transactions on Geoscience and Remote Sensing*, *60*, 1-13. doi: 10.1109/TGRS.2022.3210868

Wegmüller, U., Werner, C., Strozzi, T., Wiesmann, A., Frey, O., & Santoro, M. (2016). Sentinel-1 support in the gamma software. *Procedia Computer Science*, *100*, 1305-1312. Retrieved from https://www.sciencedirect.com/science/article/pii/S1877050916324152 (International Conference on ENTERprise Information Systems/International Conference on Project MANagement/International Conference on Health and Social Care Information Systems and Technologies, CENTERIS/ProjMAN / HCist 2016) doi: https://doi.org/10.1016/j.procs.2016.09.246

Wright, T. J., Parsons, B., England, P. C., & Fielding, E. J. (2004). Insar observations of low slip rates on the major faults of western tibet. *Science*, *305*(5681), 236-239. Retrieved from `https://www.science.org/doi/abs/10.1126/science.1096388` doi: 10.1126/science.1096388

Xu, X., Sandwell, D. T., Klein, E., & Bock, Y. (2021). Integrated Sentinel-1 InSAR and GNSS time-series along the San Andreas fault system. *Journal of Geophysical Research: Solid Earth*, *126*(11), e2021JB022579. Retrieved from `https://agupubs.onlinelibrary.wiley.com/doi/abs/10.1029/2021JB022579` (e2021JB022579 2021JB022579) doi: https://doi.org/10.1029/2021JB022579

Yang, Q., Zhao, W., Dixon, T., Amelung, F., Han, W., & Li, P. (2015, October 1). InSAR monitoring of ground deformation due to CO2 injection at an enhanced oil recovery site, West Texas. *International Journal of Greenhouse Gas Control*, *41*, 20–28. (Publisher Copyright: © 2015 Elsevier Ltd.) doi: 10.1016/j.ijggc.2015.06.016

Yu, C., Penna, N. T., & Li, Z. (2017). Generation of real-time mode high-resolution water vapor fields from GPS observations. *Journal of Geophysical Research: Atmospheres*, *122*(3), 2008-2025. Retrieved from `https://agupubs.onlinelibrary.wiley.com/doi/abs/10.1002/2016JD025753` doi: https://doi.org/10.1002/2016JD025753

Zebker, H. A. (2017). User-friendly insar data products: Fast and simple timeseries processing. *IEEE Geoscience and Remote Sensing Letters*, *14*, 2122-2126.

Zebker, H. A., Rosen, P. A., & Hensley, S. (1997). Atmospheric effects in interferometric synthetic aperture radar surface deformation and topographic maps. *Journal of Geophysical Research: Solid Earth*, *102*(B4), 7547-7563. Retrieved from `https://agupubs.onlinelibrary.wiley.com/doi/abs/10.1029/96JB03804` doi: https://doi.org/10.1029/96JB03804

Zebker, H. A., & Villasenor, J. (1992). Decorrelation in interferometric radar echoes. *IEEE Transactions on Geoscience and Remote Sensing*, *30*(5), 950-959. doi: 10.1109/36.175330

Zebker, M. S., Chen, J., & Hesse, M. A. (2023). Robust surface deformation and tropospheric noise characterization from common-reference interferogram subsets. *IEEE Transactions on Geoscience and Remote Sensing*, *61*, 1-14. doi: 10.1109/TGRS.2023.3288019

Zhai, G., Shirzaei, M., & Manga, M. (2021, 05). Widespread deep seismicity in the Delaware Basin, Texas, is mainly driven by shallow wastewater injection. *Proceedings of the National Academy of Sciences*, *118*, e2102338118. doi: 10.1073/pnas.2102338118

Zheng, Y., Fattahi, H., Agram, P., Simons, M., & Rosen, P. (2022). On closure phase and systematic bias in multilooked SAR interferometry. *IEEE transactions on geoscience and remote sensing*, *60*, 1-11.

Zheng, Y., Zebker, H., & Michaelides, R. (2021). A new decorrelation phase covariance model for noise reduction in unwrapped interferometric phase stacks. *IEEE Transactions on Geoscience and Remote Sensing*, *59*(12), 10126-10135. doi: 10.1109/TGRS.2021.3050087

Zheng, Y., & Zebker, H. A. (2017). Phase correction of single-look complex radar images for user-friendly efficient interferogram formation. *IEEE Journal of Selected Topics in Applied Earth Observations and Remote Sensing*, *10*, 2694-2701.

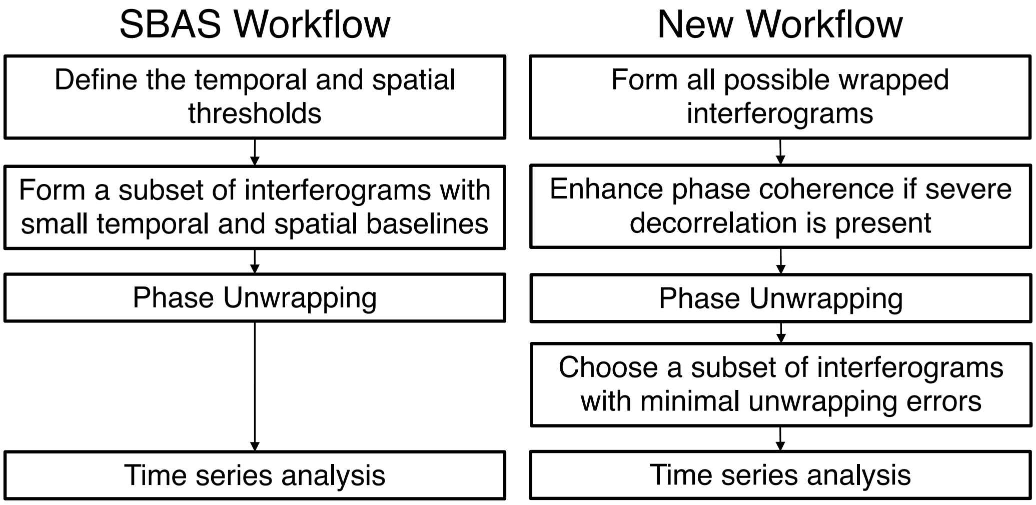

Figure 1. (Left) SBAS InSAR time series analysis workflow. (Right) The new workflow that first mitigates decorrelation noise through InSAR phase reconstruction, then selects the an interferogram subset based on the quality of InSAR phase measurements for time series analysis.

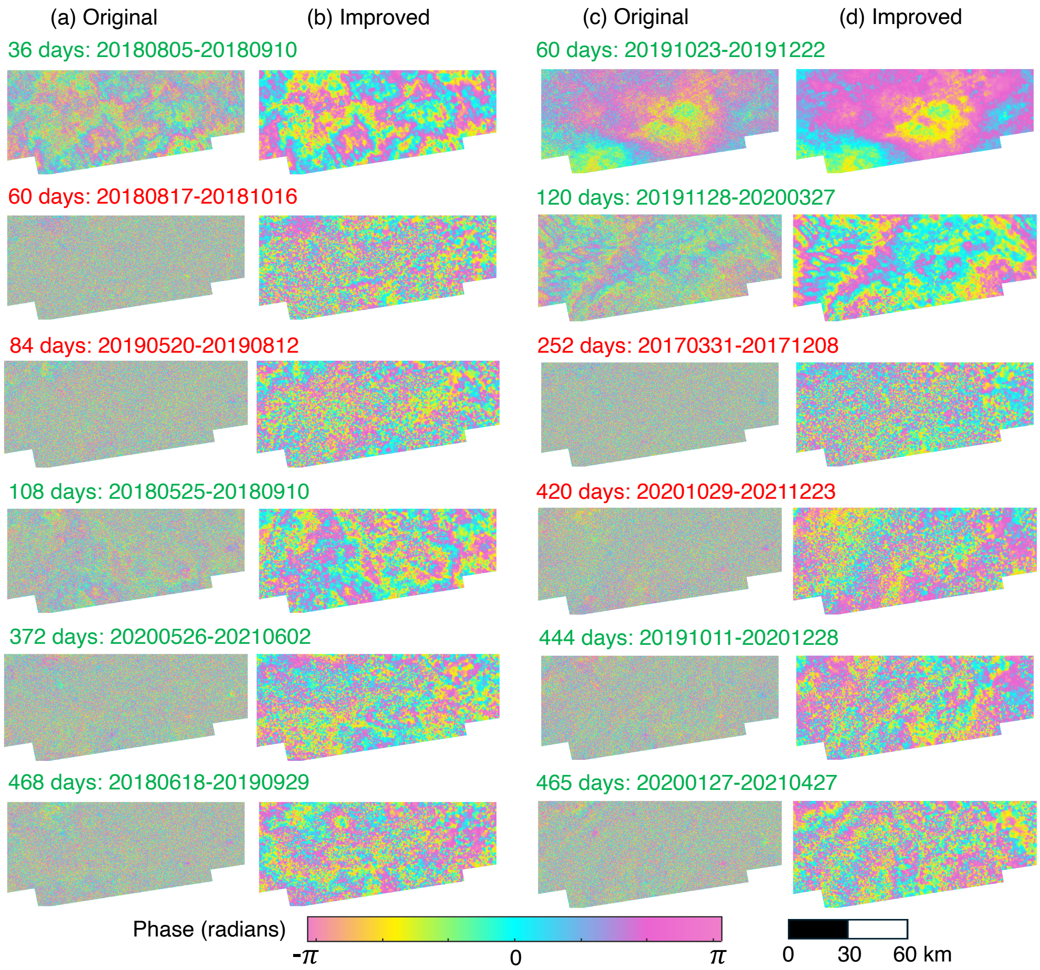

Figure 2. Examples of original interferograms (columns a and c) and reconstructed interferograms (columns b and d) over the Eagle Ford region with varying temporal baselines. Columns a and b use summer Sentinel-1 acquisitions, while columns c and d use Sentinel-1 winter acquisitions. The reconstructed interferograms marked in green were included in the final subset for time series analysis, and the interferograms marked in red were discarded due to relatively large phase unwrapping errors.

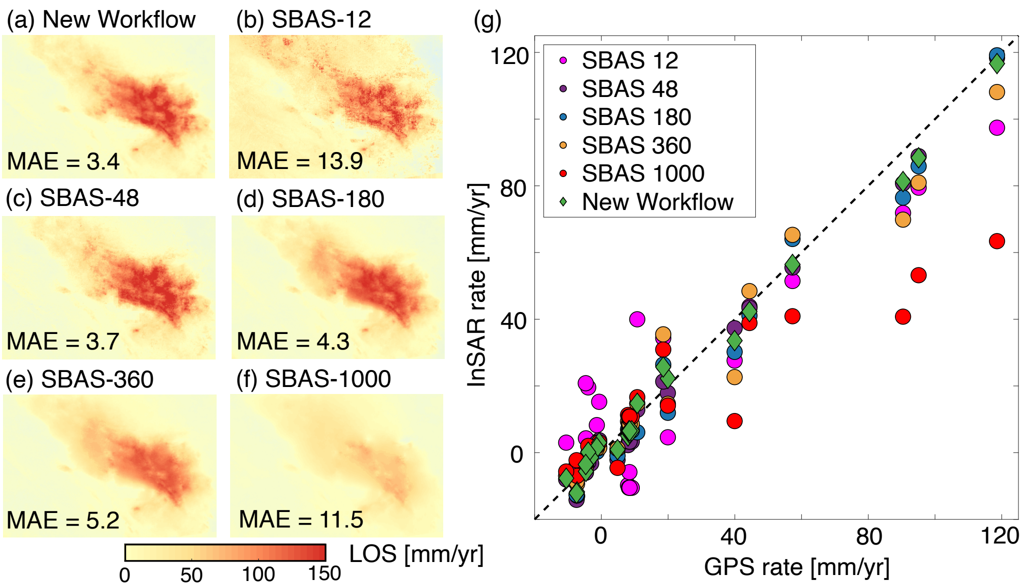

Figure 3. Cumulative line-of-sight (LOS) deformation over the Tulare Basin from 2017-2021 as derived from: (a) a subset of phase reconstructed interferograms with small phase unwrapping errors; and (b-f) a subset of original interferograms with temporal baseline thresholds of 12, 48, 180, 360, and 1000 days. The mean absolute error (MAE) difference of the linear rate estimate (mm/yr) between 24 InSAR and GPS stations over the time period is marked on each deformation solution. Subsidence causes positive LOS deformation (red). (g) Scatter plots of co-located GPS and InSAR LOS deformation rate estimates (mm/yr) derived from different interferogram subsets.

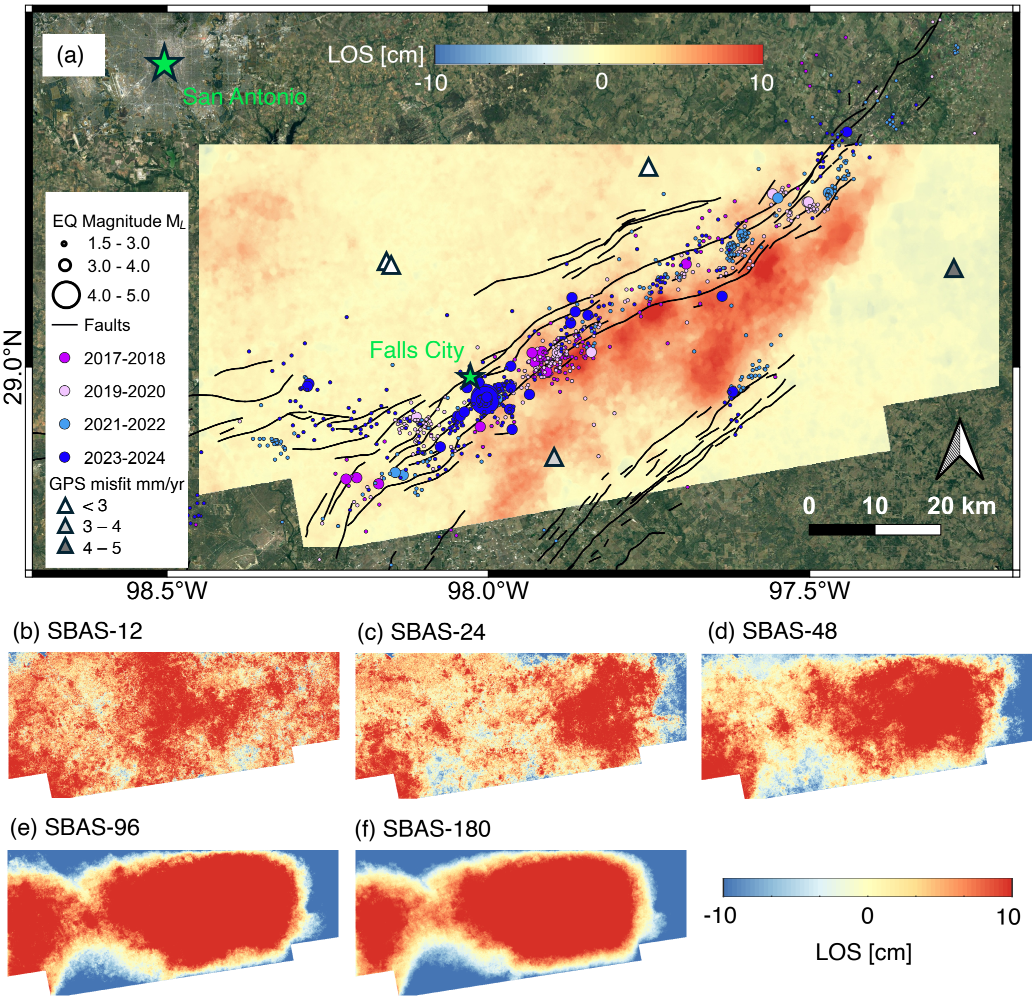

Figure 4. Cumulative line-of-sight (LOS) deformation over the Eagle Frod region between February 2017-December 2021 as derived from: (a) a subset of phase reconstructed interferograms with small phase unwrapping errors. Subsidence leads to positive LOS deformation. The locations and magnitudes of earthquakes since 2017 (circles), mapped faults are from McKeighan et al. (2022), and GPS stations (triangles). A cluster of recent earthquakes (M_L>4.0) occurred near Falls City; and (b-f) original decorrelated interferograms with temporal baseline thresholds of 12, 24, 48, 96, and 180 days.

Supporting Information for "A robust method for selecting a high-quality interferogram subset in InSAR surface deformation analysis"

M. S. Zebker [1] *, J. Chen[1,2]

[1]Jackson School of Geoscience, Department of Earth and Planetary Science, The University of Texas at Austin, Austin, TX

[2]Department of Aerospace Engineering and Engineering Mechanics, The University of Texas at Austin, Austin, TX

Contents of this file

Corresponding author: M. S. Zebker, Department of Earth and Planetary Science, The University of Texas at Austin, Austin, TX, 78712, USA. mzebker@utexas.edu

*Austin, TX

April 10, 2024, 10:50pm

S1. Residual tropospheric noise in Small BAseline Subset solutions

Under the assumption that tropospheric turbulence noise is the primary error source, the observed InSAR phase, $\Delta\phi$, at a pixel of interest can be defined as:

$$\Delta\phi = \frac{4\pi}{\lambda}(\Delta d + \Delta n) \tag{1}$$

where λ is the radar wavelength, Δd is the line-of-sight (LOS) deformation between the two radar acquisition times, and Δn is the tropospheric turbulence noise at this pixel location.

Given M SAR acquisitions, we can form N high-quality interferograms. To compute the average velocity, v_c, over the study period, we define an SBAS system of N equations as:

$$BPv_c = \Delta\Phi \tag{2}$$

where B is the $N \times (M-1)$ system matrix as defined in Berardino, Fornaro, Lanari, and Sansosti (2002). P is a $(M-1) \times 1$ vector of ones, and $\Delta\Phi = [\Delta\phi_1, ..., \Delta\phi_N]^T$ is a $N \times 1$ vector of observed phases at the pixel of interest. The least squares solution for v_c is:

$$\begin{aligned} v_c &= \frac{\lambda}{4\pi \sum_i^N \Delta t_i^2} \sum_i^N \Delta t_i \Delta\phi_i \\ &= \frac{\lambda}{4\pi \sum_i^N \Delta t_i^2} \sum_i^N \Delta t_i \Delta d_i + \frac{\lambda}{4\pi \sum_i^N \Delta t_i^2} \sum_i^N \Delta t_i \Delta n_i \end{aligned} \tag{3}$$

where Δt_i is the temporal baseline of the interferogram i. The residual tropospheric noise, r_n, in the SBAS constant velocity solution is:

$$r_n = \frac{\lambda}{4\pi \sum_i^N \Delta t_i^2} \sum_i^N \Delta t_i \Delta n_i \tag{4}$$

A smaller noise residual leads to a more accurate velocity solution. Based on Eq. 4, the residual tropospheric noise is smaller when interferograms with longer temporal baselines are used as input in the SBAS inversion. For example, for the same N, the residual tropospheric noise is four times smaller if all interferograms span 48 days instead of 12 days. Furthermore, the residual noise tends to decrease when N increases, given that tropospheric turbulence noise can be considered random over time.

References

Berardino, P., Fornaro, G., Lanari, R., & Sansosti, E. (2002). A new algorithm for surface deformation monitoring based on small baseline differential SAR interferograms. *IEEE Transactions on Geoscience and Remote Sensing*, *40*(11), 2375-2383. doi: 10.1109/TGRS.2002.803792

Table S1. Time (in seconds) required for unwrapping original and reconstructed interferograms (Fig. 2) over the Eagle Ford site.

Interferogram	Original	Reconstructed
20180805-20180910	1	1
20180817-20181016	227	9
20190520-20190812	178	5
20180525-20180910	83	1
20200526-20210602	147	2
20180618-20190929	181	3
20191023-20191222	<1	1
20191128-20200327	2	1
20170331-20171208	209	19
20201029-20211223	165	3
20191011-20201228	156	2
20200127-20210427	192	5

Table S2. InSAR-GPS line-of-sight misfit (mm/yr) for different deformation solutions at 24 California GPS stations.

GPS Station	New Workflow	SBAS-12	SBAS-48	SBAS-180	SBAS-360	SBAS-1000
CACO	3.7	15.9	4.4	2.3	2.1	3.8
CAD1	-3.0	-17.8	-5.7	-1.0	1.4	3.3
CAFP	-0.8	-5.8	-1.8	6.8	8.0	-16.4
CAHA	-9.1	-18.6	-9.7	-14.0	-20.6	-49.6
CAKC	2.9	9.6	4.4	1.6	2.7	3.3
CAWO	-4.5	1.2	-5.9	-5.6	-2.1	0.3
CRCN	-1.9	-21.2	-0.2	0.6	-10.5	-55.2
DLNO	-2.5	-14.2	-4.3	-1.2	0.2	1.7
GR8R	-1.0	8.9	-1.3	0.6	0.6	2.4
LEMA	-6.7	-15.6	-6.2	-9.2	-14.1	-41.9
MULN	-2.1	-0.6	-1.0	-3.3	4.0	-5.5
P056	-6.4	-12.3	-2.6	-9.7	-17.3	-30.5
P300	1.6	3.6	-0.2	2.5	2.9	4.5
P302	4.1	23.5	1.0	3.6	3.5	6.0
P304	4.0	29.2	2.1	-4.7	3.9	5.9
P541	2.9	13.5	2.5	3.6	3.5	4.9
P547	1.1	25.5	-1.3	0.7	0.3	1.3
P564	2.3	-15.3	-2.0	-8.0	-5.3	-5.8
P565	-1.7	-18.8	-4.9	-1.6	0.4	2.5
P566	-3.9	-4.5	-7.0	-5.8	-3.7	-9.4
P809	-2.6	-19.6	-5.8	-2.5	-0.5	1.7
P810	-1.9	-19.0	-5.2	-1.8	0.2	2.3
RAPT	-4.7	3.8	-6.7	-5.2	-1.3	5.2
TRAN	7.1	15.8	2.8	7.8	16.9	12.4
MAE	3.4	13.9	3.7	4.3	5.2	11.5

Table S3. InSAR-GPS line-of-sight misfit (mm/yr) for different deformation solutions at 5 Texas GPS stations.

GPS Station	New Workflow	SBAS-12	SBAS-24	SBAS-48	SBAS-96	SBAS-180
LCNX	-2.4	-1.3	1.5	-8.6	-14.1	-13.9
TXCU	4.8	-16.0	12.5	28.1	35.3	34.7
TXKC	3.5	0.1	4.9	12.6	13.2	16.8
TXFV	0.7	2.8	-0.3	0.0	-1.1	-0.7
TXFI	2.1	-7.4	-4.3	-2.8	-1.0	0.5
MAE	2.7	5.5	4.7	10.4	12.9	13.3

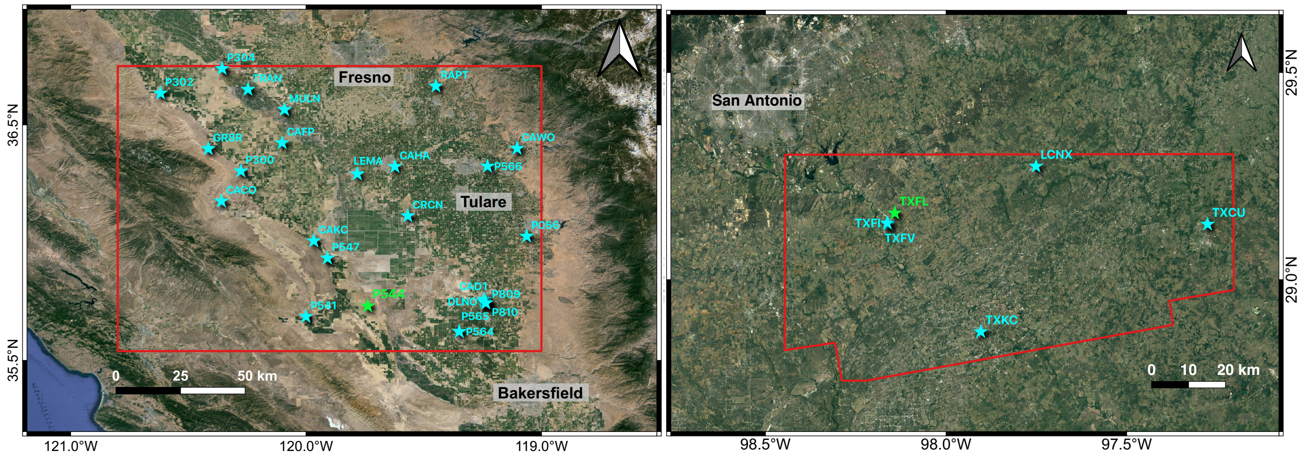

Figure S1. (Left) Tulare Basin and (Right) Eagle Ford study sites. The radar footprints are outlined in red, the reference GPS stations are shown as green stars, and GPS validation stations are shown as blue stars.

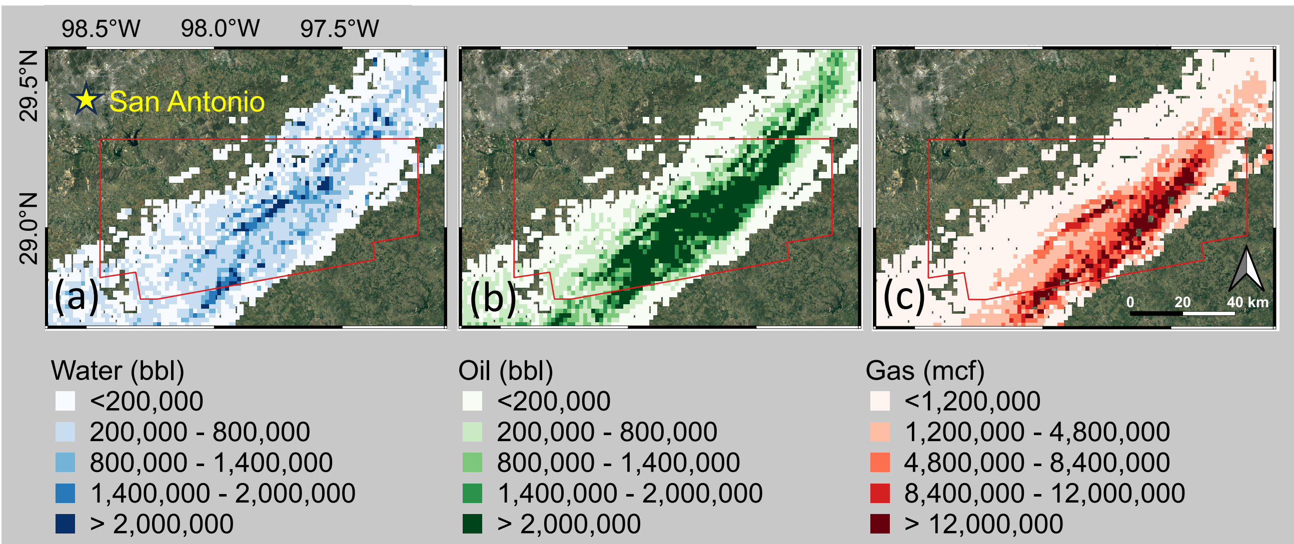

Figure S2. Cumulative water, oil, and gas production over the Eagle Ford region from 1974-2022, where over 90% of total production has occurred since 2010. The outline of the radar footprint is in red. Produced water, oil, and gas data provided by Center for Injection and Seismicity Research (CISR) at The University of Texas at Austin, Bureau of Economic Geology (BEG).

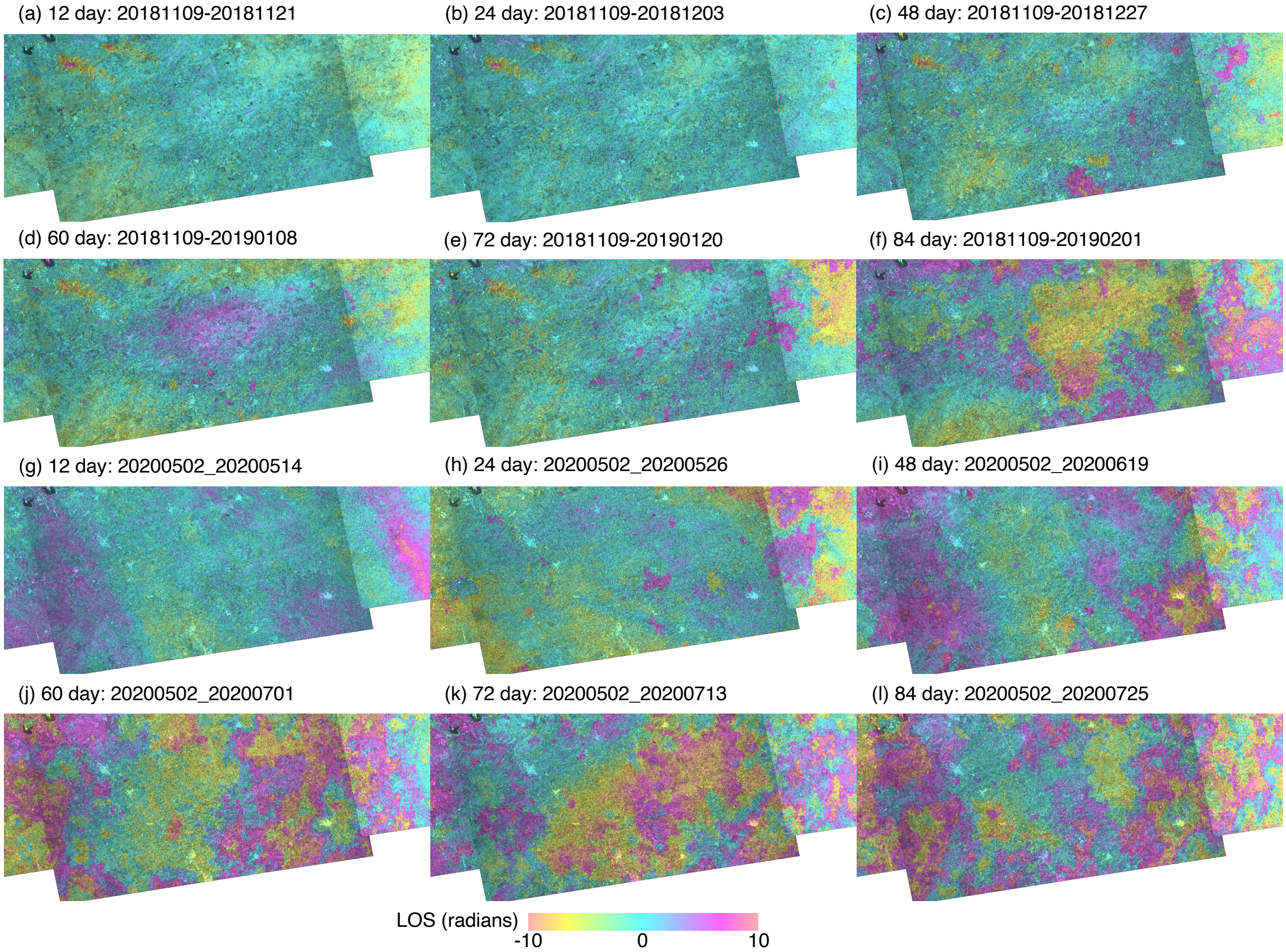

Figure S3. Eagle Ford interferograms that span the winter months (a-f) and summer months (g-l) with varying temporal baselines. Over the winter months, unwrapping errors occur in interferograms that span 48 days or longer, while over the summer months, unwrapping errors occur in interferograms that span 24 days or longer.